Nano reinforced cement paste composite with functionalized graphene and pristine graphene nanoplatelets

Tanvir S Qureshi[a], Daman K Panesar[a*],

[a] Department of Civil and Mineral Engineering, University of Toronto, Toronto, Ontario M5S 1A4, Canada

*Corresponding author: e-mail: d.panesar@utoronto.ca; Tel.: +1-416-946-5712

Abstract

This study examines and compares the workability, hydration, mechanical, microstructure and transport properties of cement paste composites containing the three forms of graphene-based 2D nanomaterials synthesized from epigenetic graphite deposit, namely, graphene oxide (GO), reduced graphene oxide (rGO), and pristine graphene nanoplatelates (G). Graphene materials were used from 0.01% to 0.16% of cement weight. The rGO and G were treated with salt and surfactant, respectively during synthesis, to improve dispersion in water. Characteristics and physical strength vary among GO, rGO and G, which have influenced the properties of nano reinforced graphene-cement composites (GCCs). The 28-day compressive and flexural strength of graphene (GO, rGO and G) cement composite improved by 28% and 81%, 30% and 84%, and 39% and 38%, respectively, compared to the control mix (cement paste without graphene materials). Finally, microscopic analysis, dynamic vapour sorption (DVS), electrical resistivity and water sorptivity results suggested that graphene materials densify and reinforce the composite microstructure.

Keywords: Graphene-cement composites (GCCs), Dispersion, Mechanical properties, Microstructures.

1. Introduction

Graphene materials are gaining attention for their potential to improve the properties of cement-based composites and concrete materials. Graphene is a single layer of carbon atoms densely packed into a benzene-ring structure. Graphene based materials are extraordinary 2D nanomaterials due to their

unique chemical characteristics and properties of high: mechanical strength, specific surface area, and electrical and thermal conductivities [1,2]. These unique properties of graphene materials have the prospects to modify the strength properties and durability performance of concrete at the nano-micro scale.

Pristine graphene in this study is termed 'G' which is a few-layer to multi-layer graphene nanoplatelets and does not have any functional groups as defects or impurities. There are two common forms of functionalized graphene-based nanomaterials, graphene oxide (GO), and reduced graphene oxide (rGO). GO is composed of graphene layers with active oxygen-containing functional groups on its surface, such as hydroxyl, epoxide, carboxyl, and carbonyl groups [3]. rGO is composed of graphene layers with a reduced level of functional groups compared to GO.

Graphene materials are commonly produced from graphite through the chemical oxidation and exfoliation of graphite layers known as *chemical reduction route* (CRR) [4], ultrasonication of graphite known as *ultrasonication route* (USR) [5], and mechanical exfoliation of graphite layers using *ball milling route* (BMR) [6]. In those processes, it is possible to produce bulk quantities (kilograms) of graphene materials [7] for large scale applications.

Different forms of graphene materials exhibit considerably different physicochemical properties due to their different molecular structure arrangement. The physical properties of GO, rGO, and G are presented in Table 1 [8]. GO is hydrophilic and electrically nonconductive. The mechanical properties of GO are reduced compared to G, due to the presence of the functional groups. Nevertheless, GO has an elastic modulus of 23-42 GPa and tensile strength of approximately 0.13 GPa [9]. rGO has an elastic modulus of 250±150 GPa [10] and is partially dispersible in water. The reduction of functional groups considerably increases the mechanical and electrical conductivity properties in rGO graphene layers. The dispersion of rGO in water depends on the reduction level of the functional groups as such, the high-level functional groups, and the high dispersion of rGO in water. Single layer G exhibits an elastic modulus of nearly 1 TPa, and tensile strength of nearly 130

GPa [11], it is also highly electrically conductive (approximately 1000 S/m) [12]. However, G is hydrophobic and not dispersible in water.

GO has been most commonly studied in the GCCs [3,13,14], owing to its high dispersibility in water, and it is reported to improve the mechanical properties of the composites. Varying dosages of GO (0.01-2.00 wt% of cement) has been investigated by various researchers aiming to understand the interplay between GO dosage and the mechanical, microstructure and transport properties of the GCCs [3,14–22]. The GCCs with 0.02 wt% GO (25.45% oxygen, layer thickness of 15 nm, and size (i.e. length or diameter of the 2D plane) 80-300 nm) was reported to have improved the tensile and flexural strengths by 197.2 and 184.5%, respectively, compared to the 100% cement paste [18]. GO having a layer thickness < 100 nm and a size of 1-2 μm with the dosage of 0.02 and 0.03 GO wt% of cement improved tensile and compressive strengths by about 13 and 41%, respectively, compared to the 100% cement mix [16]. About 0.05 wt% of GO with a 35% oxygen and 1 nm layer thickness in the presence of a superplasticizer enhanced the compressive and flexural strengths of the GCCs by 40% and 70%, respectively. A relatively high volume percentage (2%) of GO (size < 2 μm and layer thickness of 1-5 nm) in the GCCs increased compressive strength and elastic modulus about 54% and 50%, respectively, compared to the 100% cement mix [22].

GO is reported to reduce the porosity of the GCCs compared to the samples without GO [13,23–29]. GO with an average plane section of 520 nm^2 and an approximate thickness of 1 nm in the GO-cement composite shows a reduction of approximately 13.5% total porosity and 27.7% capillary pores (10 nm - 10 μm) and 100% increase in gel pores (d < 10nm), compared to that of 100% cement samples [28]. Gel pore volume in the cement paste is related to the CSH gel content. Hence, an increase of the gel pore volume in the GO-cement composite indicates an increase in CSH gel content which densifies the composite matrix.

The transport properties of the GCCs are reported to be modified by GO [3,13,17,23]. The GO-cement composites have higher electrical resistivity and lower sorptivity compared to the 100% PC paste [3]. The electrical resistivity measurement at early ages, i.e. 24 h in the GO-cement composite

also increases compared to the 100% cement mix [17]. The ingress of chloride ions is also reported to be reduced in the GO mortar composites [23].

Despite recent progress, studies have reported contradictions on the effectiveness of GO in the GCCs. This is principally owing to the challenges associated with effective dispersion of GO in the composite, consistent and efficient mixing protocol, lack of understanding of graphene materials characteristics, difference in graphene materials synthesis process and graphite source. Researchers have collected GO or graphite for GO synthesis from commercial sources [16–18,23–25,28,30–33] with limited or no information on the purity and grade of graphite which may impact the GCCs properties. For example, the mechanical properties were improved greater in Qiu et al. [18] compared to Mokhtar et al. [16] despite similar GO dosage (0.02 wt.% of cement), water to cement ratio (0.30), curing regime and age. Another study reported that the hydration kinetics of the cement is not strongly influenced by the GO with a thickness of 0.86 nm [25]. Then again, GO was reported to accelerate the degree of hydration of Portland cement (PC) paste systems [18]. According to Lv et al. [12], GO with oxygen 29.75%, thickness 8 nm, and size 80-260 nm, encouraged the formation of flower-like crystals during the hydration of the GCCs which have substantially improved the mechanical strength of the composite. However, Cui et al. [19] contradict these findings, particularly due to the scanning electron microscopy (SEM) sample preparation method, because the flower-like crystals, they suggest, could be the carbonation products of the cementitious hydrates.

Few studies reported the influence of rGO in the GCCs [4,19,20,34]. The 28-day flexural strength increased by 23% in a GCC with 0.02 wt% rGO of cement, compared to the 100% cement paste [20]. About 0.35 wt% rGO of fly ash cement in the composite increased the flexural strength, Young's modulus and flexural toughness by 134%, 376%, and 56%, respectively, compared to the fly ash cement paste without rGO [19]. Qureshi and Panesar (2019) examined a commercial graded rGO having a C:O ratio of ~82:18, ***d*** spacing of 0.36 nm and size of 17.5±9.2 μm in a 0.06 wt% of cement in the composite which shown an increase in the compressive strength and flexural strength by 15% and 33.7%, respectively, compared to the 100% cement paste [34]. Nevertheless, the mechanical strength performance of the rGO composite considerably varies with the reduced level of functional

groups compared to the GO composites [4]. Hence, this is important to characterize and specify the exact forms of rGO while used in the GCCs.

The porosity and transport properties also can be modified by rGO in the GCCs. Micropores (~0.5 μm) in the rGO composite has also been reported to fill with rGO sheets [19]. The presence of rGO in the GCCs decreased water sorptivity and mass porosity in 7 days then, both properties increased by 28 days [20], compared to the control mix. In Qureshi and Panesar's study [34], the water sorptivity was found reduced by about 4.7% by 0.06 wt% rGO of cement in the composite, compared to the control mix (100% PC).

The investigation of G in the GCCs is limited, in the literature, possibly owing to its hydrophobic behavior. The GCCs of 0.03 wt% G was reported to increase the flexural strength by 40% compared to the 100% cement paste [35]. A GCCs with PC and graphene of 6-60 μm size and 90% carbon composition reported to kept a compact structure under 500 ^{o}C while investigated for thermal resistance under high temperature [36]. A cement mortar composite with PC and 0.5 wt% plasma-functionalized graphene of size <20μm and layer number <20 reported to increased compressive strength by 56%, compared to the 100% PC mortar [37]. Nevertheless, the agglomeration of pristine graphene in water is a common limitation at the nanoscale [11], and no apparent solution of this challenge has been found which limits the development of G GCCs.

All these discussed studies on the GO, rGO, and G reinforced GCCs show the potential for improving the mechanical properties and microstructure, yet there are existing research gaps. Firstly, the efficient processing of different graphene materials and techniques for dispersion in water and cement paste system needs to be developed for consistent improvement of the composite properties. Secondly, critical graphene material parameters, such as size, layer thickness, numbers of layers, C:O ratio, functional groups, surface chemistry, and ***d*** spacing, as well as physical strength need to be utilized to explain their influence on the GCCs. Thirdly, the cement hydration process, strength and nano-microstructural development, and transport properties of the GCCs with different graphene forms of graphene materials require direct comparison.

To address the existing research gaps, the objective of this study is to establish a fundamental understanding and a direct comparison of GO, rGO, and G in the nano reinforced GCCs. This study reports the synthesis of GO, rGO and G nanomaterials from an epigenetic graphite deposit, in-depth characterization, improved dispersion technique in the water, and investigate the direct comparison of their influence on the properties of GCCs.

2. Materials and methods

2.1 Materials

General use PC was supplied by CRH Mississauga plant, and its chemical composition is shown in Table 2. High-Purity graphite (99.9% Cg) was supplied by Zenyatta Ventures Ltd. after purification from the Albany graphite deposit which is located in northeastern Ontario (Canada). Albany graphite deposit is a unique example of an epigenetic graphite deposit. Further information on the epigenetic graphite deposit and synthesis of graphite is reported in [3]. Three forms of graphene materials (GO, rGO, and G) were produced from purified graphite (Fig. 1) with the intended application in the nano reinforced GCCs. GO, and rGO were synthesised using the CRR process, and G was synthesised using liquid-phase exfoliation through USR process.

2.2 Synthesis of graphene oxide (GO), reduced graphene oxide (rGO) and pristine graphene (G)

GO was synthesised through the CRR process following the modified hummers method with some modifications [3,38,39]. Briefly, 10.0 g of high-purity graphite powder was added into a mixture of 900 mL H_2SO_4 and 100 mL H_3PO_4, and this reaction mixture was vigorously stirred at 50 °C for 2 h. Then 45.0 g of $KMnO_4$ was added, and the mixture was stirred for 15 h at 50 °C. The mixture was subsequently transferred into a 1 L ice bath containing a reaction container with 50 mL H_2O_2. The solid-state of GO mixture was then isolated by centrifugation. The solid GO mixture was then thoroughly rinsed with water, HCl (30 wt.%), and ethanol, and then soaked in diethyl ether. Finally, the resulting solid GO was washed with water to produce 30 mg/mL GO dispersion in water.

For the synthesis of reduced graphene oxide (rGO), 10.0 g of GO was dispersed in 2.0 L water (5 mg/ml) using ultrasonication. The pH of the GO dispersion was adjusted to 9 with sodium carbonate. The reaction mixture was then heated to 80 °C. Then, 100.0 g of sodium borohydride ($NaBH_4$) was slowly added to the reaction mixture and maintained reaction temperature at 80 °C for 2 hr. The reaction mixture was then allowed to cool to room temperature. Reduced graphene oxide (rGO) was separated from the reaction mixture using centrifugation and rinsed with water. Finally, the rGO was dried for 16 hr at 70 °C.

A pristine graphene-based aqueous suspension was prepared by exfoliating graphite by ultrasonication (Cole-Parmer RK-04711-60 tip sonicator, 1-hour processing) in a water solution of poly (ethylene glycol)-block-poly (propylene-glycol)-block-poly (ethylene glycol) (PEG-PPG-PEG) triblock copolymer. The direct ultrasonication of graphite in the presence of a suitable surfactant solution in the USR process is a viable process for producing high purity G since in the CRR process it is not possible to synthesize completely defect free graphene layers. PEG-PPG-PEG has been demonstrated to exfoliate graphite into high concentration aqueous dispersions of few-layer and multilayer graphene nanoplatelet [40,41]. The raw hydrothermal vein graphite used in this process has a flake diameter of 17.5 μm. Raw graphitic materials (i.e. a soft crystalline form of carbon, composed of graphene layers) were exfoliated using PEG-PPG-PEG at three different polymer chain lengths: i) Pluronic® L-31, BASF Co., average molecular weight Mn = 1,100 amu; ii) Pluronic® P-123, BASF Co., average molecular weight Mn = 5,600 amu; and iii) Pluronic® P-123, BASF Co., Mn = 14,600 amu. In all cases, PEG-PPG-PEG was dissolved at 0.4 mg/mL in deionized water. This produces a black ink in water with minimal residual upon 12 hr of sedimentation.

2.3 Characterisation of graphene materials

A field-emission SEM (JEOL JSM-6610LV) equipped with Energy Dispersive X-ray analysis (EDX) was used to characterise the morphology and surface composition of the graphene materials. Agilent atomic force microscope (AFM) and Witec Alpha 300S atomic force microscope were employed to

analyse and measure the thickness of the graphene flakes. A Philips PW 3710 X-ray diffractometer with Ni-filtered monochromatic Cu-K_α radiation source (1.5406 Å, 2.2 KW Max) was employed for the X-ray diffraction (XRD) analysis. To quantify the defect density of the synthesized samples, a micro-Raman analysis was performed using a 532-nm laser excitation using a Bruker SENTERRA dispersive Raman microscope. A Thermo Scientific iS50 Fourier-transform infrared spectroscopy (FTIR) was used to investigate the vibrational stretching modes of different molecular bonds to compare the changes of the oxygen functional groups in graphene materials.

2.4 Dispersion of graphene materials in water

Graphene materials (GO, rGO and G) were dispersed in deionised water prior to mixing with cement. The initial dispersion pattern of graphene materials just after mixing with deionised water is available in the Supplementary video file-1. It could be noted in the dispersion video that both the GO and G aqueous suspension were started dispersing in deionised water just after initial mixing. Dry rGO powder was also efficient in dispersing after initial mixing, and a little stirring seems to be considerably improved the dispersion. To make sure efficient dispersion of all three graphene materials in deionised water, following steps were followed after initial mixing: (i) graphene materials were first mixed with deionized water for 3 hr at 1000 rpm, (ii) the mixture was sonicated using a bath sonicator for 3 hr and left for 18 hr, and (iii) the mixture was stirred for 1 hr and sonicated for 1 hr prior to mixing with cement.

Supplementary video related to this article can be found at https://doi.org/10.1016/j.compositesb.2020.108063

Photographs taken after the dispersion of graphene materials and prior mixing in the cement composites are presented in Fig. 2. The dispersion of GO, rGO, and G in water was considered to be similar after mixing based on the visual observations. No visible solid residue was observed at the bottom of the beaker upon 18 hr sedimentation, which was desirable to confirm the efficient water dispersion of all the three graphene materials.

The pH of the water after dispersing graphene materials are presented in Table 3. GO dispersed water was acidic due to GO's functional groups and acids used during the GO synthesis process. Increasing proportions of rGO increase the pH of the solution up to 10.24 (in 0.16% rGO) since rGO is alkaline due to the use of sodium carbonate and sodium borohydride during the rGO reduction process. However, both sodium carbonate and sodium borohydride improved the dispersion of rGO in the water which was highly desirable. The pH in the G dispersed water varies between 6.09 and 6.96. G had a minor impact on the pH value of the water due to the effect of PEG-PPG-PEG used for G suspension synthesis during the liquid-phase exfoliation. The PEG-PPG-PEG considerably improved the dispersion of G in the water (see Supplementary video file-1).

2.5 Graphene-cement composite mixing and casting

One control mix with 100% cement paste and 15 batches of the GCCs with GO or rGO or G dosage between 0.01 to 0.16 wt% of cement, were prepared as presented in Table 4. Cubes (50x50x50 mm), cylinders (50 mm diameter x 100 mm height), and prisms (25x25x100 mm) of the GCCs were cast following ASTM C1738 [12] using a high-shear mixer. The well-dispersed GO, rGO, and G in water might not confirm the subsequent dispersion in the cement matrix owing to the agglomeration possibilities in the high pH cement paste environment. Hence, high shear mixing procedure was deployed to avoid any agglomeration possibilities. First, the water and graphene materials (GO, rGO and G) solution was premixed at 100-200 rpm for 15 s. The cement was then mixed for 30 s, and the mixing speed was increased to 4,000 rpm and continued for 60 s. The mixing was stopped for 30 s while the paste from the surface of the container was collected. Finally, the mixing continued at 12,000 rpm for 30 s, stopped for 15 s and then started again at 12,000 rpm for 30 s. The high-shear mixer facilitates uniform dispersion of graphen based materials in the cement paste during mixing.

Triplicates of all of the samples were prepared for each test in order to present the corresponding statistics. After casting, the samples were stored at a relative humidity > 90% and a temperature of 23±1 ºC. Specimens were demoulded after 24 hr and submerged in water at a temperature of 23±1 ºC until testing.

2.6 Graphene-cement composite testing procedures

This section describes the test procedures conducted on the GCCs. The experimental program included tests of workability, hydration kinetics, mechanical properties, microstructural analysis, and transport properties.

2.6.1 Measurement of workability

The workability of the composite paste was measured using a mini-slump test. The static and dynamic flows of the composites were measured according to Collins et al. [42] and ASTM C1437-07 [43], respectively. However, during the dynamic flow measurement, the table was raised and dropped 15 times in about 9 s whereas the standard specifies 25 times in 15 s. The number of times the table was dropped was reduced to avoid the spreading of the paste beyond the diameter of the table (~25 cm). The flow diameter was determined by averaging two diameters of slump perpendicular to each other.

2.6.2 Early age hydration

The calorimetric study was conducted on ~6 g cement paste samples using a thermometric TAM air calorimeter at a temperature of 23±1 °C. The samples were collected immediately from the same mix that was prepared externally using a high-shear mixer for casting cube, cylinder and prism specimens. The calorimeter began to record heat release data from 6±1 min after the cement was in contact with water or solution with graphene materials. The heat released from the hydration was monitored every 60 s for 72 hr, and the measured data were normalised by sample mass.

2.6.3 Mechanical properties

The mechanical properties that were tested are compressive strength and flexural strength. Three samples were tested for each property to report the mean and standard deviation. The compressive strength test was performed on 50 mm cubes according to ASTM C109 [44] using a Forney 440 kN compression testing machine at a loading rate of ~2.4 kN/s. The flexural strength test on prisms (25x25x100 mm) was performed using an Autograph AG-I, Shimadzu 50 kN testing machine

following ASTM C348 [45]. The displacement rate was 0.1 mm/min, and the span length of prisms was 75 mm.

2.6.3 Characterisation of microstructure

The microstructure of composites was analysed using Thermogravimetric Analysis (TGA), XRD, SEM and fluorescence optical microscopy on thin section, and DVS analysis. The samples for analysis were collected by cutting the prisms at 28 days. The samples were immediately treated with acetone for about 2-3 hr to restrict further hydration.

For TGA and XRD testing, samples were ground to pass the 45 µm mesh sieve and were treated with acetone for 2 days followed by vacuum oven drying for 2 days at 38 ^{o}C and put into a vacuum desiccator with silica gel for one day prior testing. The calcium hydroxide (CH) content was measured by the TGA using a Netzsch thermische analyse STA 409 cell. The test was started at room temperature ~25 ^{o}C and increased to 1000 ^{o}C over 1 h 42 m. The XRD was measured using a Philips PW 3710 x-ray diffractometer with a Cu-K_{α} radiation source. The diffractometer was operated at 30 kV and 40 mA, and emitted radiation at a wavelength of 1.5405 Å. The scanning ranged between 5-70° of 2θ at a rate of 1.25 s/step and a scanning resolution of 0.02 ^{o}/step. Following the scanning, the raw diffraction data was located in the PDF-2004 database to identify peaks in the XRD pattern using X'pert Highscore software, and phase quantification was conducted using Rietveld analysis.

Thin sections of samples were prepared from 28-day hardened cement paste composite for the fluorescence optical microscopy and back-scattered electron (BSE) image analysis. The fluorescence optical microscopy images were taken using an optical microscope, and the BSE images were taken using a JEOL JSM-6610LV SEM machine. The thin section preparation and imaging process is described in [46]. The thin section fluorescence microscopic and SEM image analysis were conducted using image-J software to examine the GCCs capillary porosity and density.

The DVS was used to investigate the meso and gel pore structure of the cement paste. The measurement was taken using a DVS Advantage-1 equipment of Surface Measurement Systems, London, UK. A description of the testing process is reported in [34]. The pore size distribution up to

22 nm diameter was calculated using the Barrett, Joyner, and Halenda (BJH) method. The specific surface area and the volume of the inner pore in the range of 0-22 nm diameter were calculated using Brunauer Emmett Teller (BET) method. The BET and BJH method calculation process is followed as described in [47].

2.6.4 Transport property tests

Electrical resistivity and water sorptivity tests were performed to analyse the transport properties of the composites as an indication of durability performance. The electrical resistivity was measured on 50 mm cubes according to the uniaxial two-electrode method described in [48,49] and using a GIATEC Scientific RCON concrete resistivity meter. Two parallel metal plates were contacted at the opposite surface of cubes and the drop in the potential between electrodes was measured while 1.2 V direct current (DC) applied at 1 kHz frequency. The electrical resistivity of the composites was monitored from 1 day to 28 days. A one-dimensional liquid capillary sorptivity test was performed on 50 mm cubes following [50]. Sorptivity testing was performed on 28-day composites after drying in a vacuum desiccator with silica gel (4 days) at a temperature of 23±1 ºC while the mass changes were 0.1% in a 24 hr period.

3. Results and discussion

3.1 Characterisation of graphene materials

Fig. 3 presents the characterisation of graphene materials using SEM-EDX, AFM, XRD, Raman spectroscopy and FTIR, and the results are summarized in Table 5. The high magnification SEM images show a thin plane formation pattern by GO (Fig. 3a), rGO (Fig. 3b) and G (Fig. 3c). The SEM image analysis indicated that the plane size of GO, rGO, and G was 2±1 µm, 4±2 µm, and 3±1 µm, respectively. The size distribution from SEM images using Origin and ImageJ analysis is available in Appendix-I. The EDX quantification confirms that the C and O contents of GO, rGO, and G are about 62-65% and 35-38%, 77-87% and 13-22%, and 99% and 0%, respectively. The EDX quantification is a close approximation approach owing to the quantification of a spot at the location of an SEM

electron beam. Similar C and O content measurements using energy-dispersive X-ray spectrometer (EDS) were reported by Lv et al. [27] and Qiu et al. [18].

The AFM images in Figs. 3d-f indicate that GO, rGO, and G were few-layer graphene materials (1-5 layers). This could be noted that few-layer GO was easily dispersed in water due to its hydrophilic nature (Fig. 3d) while rGO and G occasionally show some level of agglomeration of layers stack in water dispersion (Fig. 3g and h). The stack thickness of GO, rGO, and G in water dispersion was up to 1-1.7 nm, 125-175 nm, and 180-230 nm, respectively. Nevertheless, the synthesised rGO and G after dispersion in water were typically a few layers. rGO and G were treated with salt and surfactant, respectively, to improve their dispersibility in water. In the case of G, graphene flakes were mostly found encapsulated into PEG-PPG-PEG aggregates that facilitate their suspension, and prevent their re-agglomeration (Fig. 3f). However, the desirable PEG-PPG-PEG concentration was diluted while the G solution was added to the deionized water. The occasional stack of rGO and G indicated agglomeration of graphene materials due to the van der Waals attraction forces between graphene planes regardless of the dispersion treatment.

Fig. 3i shows the XRD pattern and the major diffraction peak at 2θ ~10.12° for GO, and a 2θ wide band around ~24.90° and 43.18° for rGO and G. The diffraction peak for rGO at 2θ ~43.18°, indicates a short-range order in rGO stacked graphene layers. For comparison, the XRD (Fig. 3i) of graphite was conducted, which shows a sharp peak cantering at 2θ ~27°. Similar XRD patterns for GO and rGO were reported in [34,51]. The ***d*** spacing between graphene layers for GO, rGO, and G calculated using the Bragg's equation are 0.85, 0.35, and 0.33 nm, respectively. The calculation procedure can be found in [3]. The ***d*** spacing increases with the oxidation of graphite to form GO, then the reduction of functional groups from GO to rGO reduces it further.

Fig. 3j shows typical D and G Raman bands of GO, rGO and G, which are located at ~1350 cm^{-1} associated with nanocrystalline carbon and ~1583 cm^{-1} associated with amorphous carbon (sp2 bonded), respectively. For G, a sharp 2D bend around ~2550 cm^{-1} was also noted. The ratio between D and G Raman bands intensity, I_D/I_G, is an efficient indicator for determining the level of functional

groups present in GO and rGO. The intensity ratio (I_D/I_G) is 0.83 for GO, while the intensity ratio of rGO, as expected, is relatively higher (0.96) and markedly lower for G (0.25). The higher intensity ratio, 0.96, of rGO indicates that the oxygen functional groups were significantly reduced compared to GO. The increase of the I_D/I_G intensity ratio from GO to rGO is related to the removal of functional groups and the formation of defects in the graphene plane [8,52]. Since there are no defects in the graphene layer, the I_D/I_G intensity ratio is low (~0.25) for G. Also the shape and position of 2D peak are consistent with few layers graphene flakes (up to 5) which are similarly reported in [53].

The FTIR graph in Fig. 3k presents the bond stretching peaks of GO for hydroxyl (-O-H at ~3220 cm^{-1}), carbonyl (C=O at 1730 cm^{-1}), aromatic (C=C at 1620 cm^{-1}), carboxy (C-O at 1415 cm^{-1}), epoxy (C-O-C at 1228 cm^{-1}), hydroxyl (C-OH at 1070 cm^{-1}). rGO demonstrated substantial losses of oxygen functional groups, in particular, hydroxyl and epoxy groups. The remaining peaks are mainly aromatic benzene C=C bond stretching and a minor stretching for carboxyl groups, which indicates the reduction of functional groups in rGO. There was no other peak found in the G in FTIR (Fig. 3k) due to the absence of functional groups. The infrared patterns are in agreement with those reported in [4,34].

The characterization parameters are summarized in Table 3. The major characterisation factors of graphene materials are: chemical structure, C and O element content (%), plane size, ***d***-spacing, layer thickness, stack thickness in water dispersion, and Raman I_D/I_G intensity ratio. For example, the functional groups are reduced in rGO compared to GO, which is indicated by the lower oxygen element (%), lower ***d***-spacing and higher I_D/I_G ratio.

3.2 Workability

Fig. 4 presents the mini-slump results of the static and dynamic flow diameter measurements of paste composites for workability study. Increasing the proportion of GO reduces both the static and dynamic flow of the GCCs compared to the control paste mix. Both the static and dynamic flow diameters were reduced by approximately 28% and 11%, respectively, in the 0.16% GO composite, compared to the control mix. This indicates that the loss of workability is proportional to the

percentage of GO in the composite paste due to the extra water required to wet their 2D plane surface. In other words, the absorption of water by the hydrophilic functional groups and high ***d***-spacing (0.85 nm) of GO in the GCCs affects its workability. Additionally, the physical interactions, such as friction between hydrophilic 2D planes of GO and cement grains may contribute to the reduced workability. However, rGO and G were treated with Na_2CO_3 and PEG-PPG-PEG surfactant, respectively, which result in similar or slightly higher static flow in the composite, compared to the control mix (Fig. 4a). Increasing the percentage of rGO in the paste reduces the dynamic flow due to the presence of remaining functional groups (Fig. 4b). rGO does extract less water from the composite since rGO is less hydrophilic compared to GO and has a low ***d***-spacing (0.35 nm). Varying the percentage of G has the least impact on the workability of the GCCs since G is hydrophobic and has the lowest ***d***-spacing (0.33 nm) compared to GO and rGO.

3.3 Hydration of composites

A calorimetric study was conducted on paste samples to analyze the impact of graphene materials on the cement hydration process. The rate and cumulative heat of hydration of the control mix and the GCC pastes recorded by the calorimeter are shown in Fig. 5. Typically two peaks generated in the rate of heat of hydration curve in the first 24 hours. The first peak evolves due to the hydration of C_3S, whereas the second peak corresponds to the hydration of C_3A phase of cement. GO accelerates the cement hydration process by increasing the rate of heat of hydration at the C_3S and C_3A hydration phases (Fig. 5a and b). The peaks of the heat flow are not only increased but also are shifted to the left, for the GO composites compared to the control mix. Acceleration of the cement hydration process by GO is also reported in similar studies [17,31]. This is due to the contribution of oxygen-containing functional groups (oxygen content 35-38%, Table 5) on the cement hydration process. The rate of cement hydration was enhanced due to the nucleation effect of graphene materials (GO>rGO>G), and intensification in the hydration range of C_3A was noted significantly, particularly in the case of GO and rGO composite mixes. Graphene oxide (GO and rGO) also can dissolute in the setting phase [54] due to their significant adsorption behaviour [55] through its functional groups. Functional groups such as –COOH on GO and rGO surface causes the diffusion of ions during the

cement hydration deceleration phase [56]. In addition, GO's functional groups may rapidly form cross-linking with a large number of ions (Na^+, K^+, OH^-, Ca^{2+}) [33] during the accelerating stage of the cement hydration process.

GO may act as nano-seeding materials promoting CSH and other hydration products which is similarly reported in [29]. rGO in the GCCs slightly delay the cement hydration and do not show much impact on heat release (Fig. 5c and d) within the first 72 hours, owing to its reduced amount of functional groups (oxygen content 13-22%, Table 5). However, the rate of heat of hydration was higher for the rGO composite compared to the control specimens, particularly during 8 to 12 hours which corresponds to the C_3A hydration phase (Fig. 5c). The rate of heat of hydration in GCCs is minimally impacted by G, compared to the control specimens as shown in Fig. 5e and f. Although there are no functional groups in G, the sp^2 bonded carbon planes of G may act as nano nucleation sites during the cement hydration process. Hence, the cumulative heat of hydration is increased in G cement paste composites compared to the control cement paste (Fig. 5f).

3.4 Mechanical properties of composites

3.4.1 Compressive strength

GO increases the compressive strength of the GCCs at all ages, compared to the control mix (Fig. 6a). The 3-day compressive strength of GO composites increased by a maximum of up to 22% and 14% compared to the control specimens, in 0.08% GO and 0.16% GO, respectively. At 14 days, increasing proportions of GO in the GCCs increases the compressive strength. The maximum 14-day compressive strength increased by 44% in 0.16% GO, compared to the control mix. However, the 28-day compressive strength of 0.04% GO, 0.08% GO and 0.16% GO were similar, and around 28% higher compared to the control mix. It is expected that PC paste gained sufficient compressive strength within 28 days and limited strength increases afterward. Hence, compressive strength enhancement due to GO addition in GCCs compared to 100% PC paste mix is expected to be stabilized by 28 days. Overall, the trend of the 28-day compressive strength of GO composites is 0.16% GO ≈ 0.08% GO ≈ 0.04% GO > 0.02% GO > 0.01% GO > control. This is principally due to

the participation of GO functional groups (oxygen content 35-38%) in the cement hydration process within the first 24 hr which enhanced hydration and reinforced the hydration compounds such as C-S-H, portlandite, and ettringite at the nano-micro scale. GO nanosheets were reported to chemically cross-linked to form bigger GO aggregates in saturated $Ca(OH)_2$ performing as fibers that successfully improved the strength and toughness properties of the GCC matrix [21]. GO layers also reported to have the ability to reinforce cracks and pores [3,14,34]. Hence, a few-layer (1-3) well-dispersed GO with an elastic modulus of 23-42 GPa have reinforced the nano-micro pores and cracks, cross-linked and increased compatible cement hydration products into the composite matrix contributing to the strength enhancement.

The 3-day compressive strength of the rGO composite increased by up to 11% in 0.04% rGO, compared to the control mix (Fig. 6b). A high proportion (>0.08%) of rGO decreased the 3-day compressive strength, compared to the control mix. However, at 14 days, increasing the percentage of rGO increases the compressive strength of the GCCs (except for 0.08% rGO) resulting in a maximum increase of 43% compressive strength in 0.16% rGO, compared to the control mix. Then again, a maximum increase in the 28-day compressive strength of the rGO composites compared to the control mix was about 30% in 0.04% rGO and 0.16% rGO. Overall, increasing the rGO concentration beyond 0.04 wt% of cement has not improved the 14-day and 28-day compressive strength of GCCs significantly. Although 0.08% rGO was expected to gain the compressive similar to that of 0.04% rGO and 0.16% rGO, the compressive strength was slightly reduced in comparison. This could be possibly owing to the materials and samples handling during this specific set of cube casting and or experimental procedures. This is due to rGO's moderately higher physical strength (elastic modulus ~ 250 GPa) and lower content of functional groups (oxygen content 13-22%) compared to GO. Chemical cross-linking of moderately high strength rGO act as nano reinforcement in the GCC matrix and improved the physical strength of the GCCs. rGO slowly influences the cement hydration process due to the reduced amount of functional groups, which reflects on the 3 and 14-day compressive strength results. The observed increase in the compressive strength of GO and rGO composites

compared to the control mix was higher at 14 days than 28 days (Fig. 6 a and b), which was similarly found in the previous study [34] and other similar works [57,58].

The G composites have a 3-day compressive strength similar to that of the control mix except for 0.02% G which had a 25% increase in compressive strength than the control mix (Fig. 6c). The 14-day compressive strength increased around 34% in 0.01% G, 0.02% G and 0.16% G, compared to the control mix. However, the 28-day compressive strength increased by about 39% in 0.02% G, compared to the control mix. The high physical strength (elastic modulus ~1 TPa and tensile strength 130 GPa) and micro size planes (0.5-5 μm) of G plays a vital role in reinforcing the GCCs matrix at a nano-micro level which improves the compressive strength properties of the GCCs. The chemical cross-linking effect might be lower between G and the hydrated cement compounds interface in the GCCs compared to GO and rGO with the hydrated cement compounds interface. However, the 2D nano planes of G may act as a nucleation site during the cement hydration process as reflected through the increase in cumulative heat of hydration (Fig. 5f) which develops good bonding between G and the cement matrix.

3.4.2 Flexural strength

The maximum flexural strength increased by 80-83% compared to the control mix, in 0.04% GO at 3 and 14-day, and 0.02% GO and 0.04% GO at 28-day (Fig. 7a). A consistent increase in the flexural strength of the GO composites compared to the control mix was due to efficient reinforcing by GO, the early age acceleration of hydration by high content functional groups, GO's consistent plane size (2±1 μm) and efficient dispersion of GO during the mixing process.

In the rGO composites, the flexural strength increased up to 43% and 52% in 0.08% rGO and 0.16 % rGO, respectively, compared to the control mix at 3 and 14-days (Fig. 7b). However, the 28-day flexural strength increased by 60%, 69% and 84% in 0.16% rGO, 0.08% rGO and 0.04% rGO, respectively, compared to the control mix. rGO slowly impacts the cement hydration process due to the low content of functional groups, which resulted in a considerable increase in the flexural strength between 14 days and 28 days. An increase in the 3-day and 14-day flexural strength of the rGO

composites, compared to the control mix, is greater when the concentration of rGO is greater, such as 0.08% and 0.16% rGO, due to rGO's moderately higher physical strength (elastic modulus ~250 GPa). The variation in rGO plane size (4±2 μm) and stack thickness (125-175 nm) also may impact the flexural strength.

In the G composites, the maximum flexural strength increased by 56-58% in 0.02 % G at 3 and 14-day, compared to the control mix (Fig. 7c). However, the 28-day flexural strength in the 0.02% G increased by 38%, compared to the control mix. Once again, this flexural strength result is caused by G's high physical strength compared to GO and rGO (Table 1) and minimal impact on the cement hydration process due to the lack of functional groups. In the first 14 days, the flexural strength increase in the G composite was high (79-94% of 28-day strength) owing to the nucleation action of the graphene plane in the cement hydration process at early ages which may not be the case between 14 and 28 days. Besides, the variation in G plane size (3±1 μm) and high stack thickness (180-230 nm) also may impact the flexural strength.

The physical strength and functional groups of graphene materials have principally influenced in the flexural strength enhancement of the GCCs. This is similarly explained in Section 3.4.1. However, graphene materials in the GCCs are more effective in improving flexural strength compared to the compressive strength which is possibly owing to the reinforcing effect of graphene materials at nano-micro scale. Nevertheless, the deviation of the mechanical properties may be due to the difference in strength development of the individual mix design specimens, instrumentation handling, variation in 2D plane size (for GO 2±1, rGO 4±2 μm, and G 3±1 μm), dispersibility, stack thickness (GO 1-1.7 nm, rGO 125-175 nm, and G 180-230 nm), and mixing efficiency during sample preparation. For example, occasional high stack thickness in rGO and G might result in lower efficiency of the nanoscale reinforcing of the composite matrix.

Overall, the physical properties and participation of graphene materials in the cement hydration process make the nanoparticles to be compatible reinforcement at nano-micro scale which increases the mechanical strength properties. Then again, different forms of graphene materials have different

mechanisms to influence the mechanical properties of the GCCs. High content of the active functional groups of GO has a vital role in the enhancement of the mechanical properties of GO composites. Both the low content functional groups and moderately high physical strength of rGO play the main function in the rGO composites' mechanical strength enhancement. In the case of G composites, both the high physical strength and nucleation effect by the 2D planes of G have a key role in the mechanical strength enhancement.

3.5 Microstructure of the composites

The TGA and XRD analysis were conducted on samples at 1, 7, 28 days. The fluorescence microscopy and SEM image analysis were conducted on 28-day thin section samples to analyse the impact of GO, rGO and G in the cement hydration process, porosity and the development of the composite microstructure. The gel porosity of the cement composites was analysed by DVS analysis.

3.5.1 Thermogravimetric analysis (TGA)

The TGA weight loss, a derivative of TG (DTG) and the mass loss for CH decomposition analysis results of the GCCs are presented in Fig. 8. The endotherms and their corresponding mass losses in Fig. 8a-c were similar to [3,34,58,59] and ascribed to: (i) at ~30-105 ^{o}C: the evaporable water and part of the bound water escapes; (ii) at ~110-250 ^{o}C: C-S-H, C_2ASH_8, Ettringite, AFm_{ss}, mono-carbonate; (iii) at ~425-500 ^{o}C: dihydroxylation of CH; and (iv) at ~650-800 ^{o}C: decarbonation of calcium carbonate. The degree of hydration of cement is directly correlated to the CH content (CH%) which was measured using the following equation as similarly described in [60]:

$$CH\% = (M_{CH}/M_{500}) \times (74/18) \times 100\ (\%)$$

Where, M_{CH} = the percentage weight loss of CH (mass loss between 425 and 500 ^{o}C), M_{500} = weight at 500 ^{o}C, and the fraction 74/18 is used to convert the CH bound water into the CH mass where 74 is the molar mass of CH and 18 is the molar mass of H_2O.

Fig. 8d presents the CH content (%) as a function of GO or rGO or G content, and time (28-day). The CH content of 28-day GO composite showed a higher degree of hydration from 0.01% GO to 0.04%

GO then decreases gradually in 0.08% GO and 0.16% GO. Although the CH content decreases 1.4% in the 0.01% GO composite compared to the control mix, the rest of the GO cement composites have a higher content of CH compared to the control mix. The maximum increase of CH content was about 0.9% in the 0.04% GO composite, compared to the control mix. Higher content of CH indicated active participation of GO's functional groups in the cement hydration process. The CH content in all of the 28-day rGO composites increased compared to the control mix. The maximum CH content increased by 2% in the 0.02% rGO, compared to the control mix. The increase in CH content of rGO composite indicates active participation of functional groups as well as nano plane action accelerating the cement hydration process. Compared to the control mix, the CH content in 28-day G composite decreased by about 0.5% in 0.01 and 0.02% G then increases in 0.04, 0.08 and 0.16% G with a maximum increase of about 0.9% in 0.08% G. Once again, the increase in CH content by G is attributed to its influence as a nano nucleation site accelerating the cement hydration process.

3.5.2 X-ray Diffraction (XRD)

The XRD patterns of the 28-day GO, rGO, and G in the GCCs are presented in Fig. 9a-c, respectively. Typical cement hydration products such as ettringite, CH, calcite, tricalcium silicate (C_3S), and dicalcium silicate (C_2S) are detected. The XRD further verified and clarified the results of hydration phases indicated by TGA. The crystalline phase intensity increases with the increasing GO, rGO and G content in the GCCs. Since XRD cannot directly detect amorphous phases, a quantitative analysis using Rietveld software was conducted on the 28-day hydrated composites to quantify the content of amorphous C-S-H gel, CH, ettringite and the relative distribution of unreacted cement. The Rietveld quantified amount of cement hydration products and unreacted cement (UC in the graph) is presented in Fig. 9d. All graphene materials reduce unreacted cement content in the GCCs compared to the control mix. The trend of the CH content in TGA is similar to the CH content in the XRD quantification. Also, the calorimetric heat release study resembles the TGA and XRD results.

Compared to the control mix, the unreacted cement content gradually decreased from 0.02% to 0.16% GO, while the amorphous content gradually increased within the same range (Fig. 9d). Although the

unreacted cement content decreased by about 3% in 0.01% GO, compared to the control mix, the CH content was quantified slightly reduced (0.8%) compared to the control mix (Fig. 9d) which is also similarly indicated in TGA results (Fig. 8d). This is due to about 3.6% increase in amorphous content in 0.01% GO, compared to the control mix. At low dosages of GO (0.01 wt% of cement), a major portion of GO may have been used in the CH to C-S-H gel conversion reactions.

The CH content in the rGO composites gradually increases with the increasing dosage of rGO in the composite except for 0.02% rGO which results in higher CH content compared to 0.04 and 0.08% rGO (Fig. 9d). In this process, the maximum CH content increased by about 1.8% in 0.16% rGO, compared to the control mix. However, maximum amorphous content increased 4.4% in 0.04% rGO, compared to the control mix then decreases in the 0.08 and 0.16% rGO pastes. Therefore, low dosages of rGO (0.01-0.04 wt% of cement) are favourable for the high content of amorphous C-S-H development in the composite matrix.

The unreacted cement and ettringite content gradually decreases, and amorphous content gradually increases with increasing dosage of G in the GCCs (Fig. 9d). No trend is noted in the CH content of G composites while 0.02 and 0.16% G shows a slight decrease in the CH content, compared to the control mix. This has been compensated by a considerable increase in the amorphous content in the 0.02 to 0.16% G composites, compared to the control mix (Fig. 9d). Therefore, it is clear that increasing the dosage of G encourages cement hydration process.

3.5.3 Microstructural image analysis

3.5.3.1 Fluorescence microscopic image analysis

A fluorescent microscopic image of the 28-day cement paste thin section was used to analyze the impact of graphene materials on the density and porosity of the composite and the corresponding ImageJ analysis is shown in Fig. 10. The fluorescence images of the GCCs, in particular, GO and rGO composites have a darker intensity compared to the G composite and the control mix (Fig. 10a, a coloured image is available in the online version for clear visual comparison). The distribution of intensity using ImageJ analysis is drawn from the normalization of 100,000 pixels (Fig. 10b-d). Lower

intensity indicates less capillary pores and a denser microstructure. Clearly, the distribution of intensity in the GO cement composite shifted to the left compared to the control mix (Fig. 10b). This shifting to the left shows a trend from 0.02 to 0.16% GO which increases with the increase in GO dosage. However, 0.01% GO's intensity distribution shows the highest shift to the left from the control mix's intensity distribution, possibly owing to the densification of the composite matrix by a high content of C-S-H as indicated in XRD quantification. The intensity distribution of the rGO composites continued to shift to the left, compared to the control mix, with the increasing dosage of rGO (Fig. 10c). This indicates the reduction of porosity in the composite by rGO action which may have been caused by the increase in the content of C-S-H, or CH, or ettringite, or the combination of those hydration compounds, as indicated by TGA and XRD results. The G composite's intensity distribution shows no apparent trend with the higher dosage of G in the GCCs (Fig. 10d). The shifting of the G composites intensity distributions to the left of the control mix distribution is also minimal compared to the GO and rGO composite.

The average intensity measured from the fluorescence microscopy images of the composites is plotted in Fig. 10e. Graphene materials, particularly GO and rGO, lower the intensity of the composite by about 36% and 47% in the 0.16%GO and 0.16%rGO composites, respectively, compared to the control mix. Increasing GO (0.02 to 0.16%) and rGO (0.01 to 0.16%) in the GCCs gradually decreases the average intensity indicating the densification of the composites. The average intensity from the ImageJ distribution curve suggests that rGO and GO results in a densified composite microstructure more than G composite specimens (Fig. 10e).

3.5.3.2 Scanning electron microscope (SEM) image analysis

Fig. 11 shows the typical BSE images of the 28-day GCCs thin section samples taken by SEM. Common cement hydration phases such as CH, ettringite and C-S-H gel materials are observed in the control specimens. The graphene materials were observed to be well distributed and densified the composite microstructure reducing the micropores. Out of the three forms of graphene materials, GO is shown to be compacted well within the C-S-H gel materials followed by rGO and G. Besides

enhancing the formation of CH and C-S-H through 2D plane nucleation effect, graphene materials to some extent may form hybrid compounds through the chemical reactions between the functional groups (for example carboxylic acid) of graphene materials and the C-S-H or CH. This is also reported in [24,31,32,58,61]. This bonding and chemical cross-linking of graphene materials with cement hydration products cause reinforcing of the composite at nano-micro scale.

The grey level thresholding of BSE images is an efficient approach for segmenting different microstructural features of cement paste composite such as hydrated and unhydrated cement compounds as well as capillary porosity. Typically the grey level histogram of a BSE image is comprised of separate peaks that correspond to the relative fractions of each phase. Hence, pores can be easily segmented since the backscatter coefficient of epoxy (0.07) that fills the pore during thin section preparation is considerably smaller than the other phases (0.12-0.19) [62]. The lower threshold levels for pores are set to zero (black pixels) in the segmentation process to separate the pores easily. In this study, the tangent-slope thresholding method was used to measure the porosity threshold in the composite according to Scrivener et al. [63], and the porosity is determined as described in [62]. The BSE images were taken from random spots avoiding air voids, and at least twenty greyscale images were collected per sample at 3000x magnification containing 2560 x 1920 pixels.

A typical porosity measuring example from the composite BSE image and measured porosity results are presented in Fig. 12. Figure 12a presents a typical BSE image (0.16% rGO) of the GCCs and the corresponding cumulative grey level histogram curve is shown in Fig. 12b. The grey value when the tangent to the upper portion of the histogram curve intersected the initial tangent on the grey level histogram provides a consistent inflexion point for determining the porosity thresholding of BSE greyscale images (Fig. 12b). Hence, the threshold value for porosity is estimated from the inflection point determined by the tangent-slope method. Fig. 12c presents the pores segmented (black pixel) image of a typical 0.16% rGO BSE image at a critical threshold level of 86 that estimated the capillary porosity of the paste composite to be ~12%. This porosity measurement technique is effective and consistent for directly measuring the porosity of the cement paste composite at the microscale.

The measured capillary porosity results from the thin section BSE images of the GCCs at 28-day are shown in Fig. 12d. The porosity of all of the graphene-cement composites is reduced compared to the control mix. Porosity in GO composite reduced by up to 1.5 and 1.8%, respectively, in the 0.01% GO and 0.16% GO composites, compared to the control mix. The porosity trend in the GO composite is 0.16% GO <0.01% GO < 0.08% GO ≤ 0.04% GO < 0.02% GO < control (Fig. 12d). This GO composite porosity trend is somewhat similar to the fluorescence microscopy image analysis result (Fig. 10). The porosity gradually reduced with the higher dosage of rGO in the GCCs, compared to the control mix (Fig. 12d). This porosity reduction trend in the rGO composite is similar to the fluorescence microscopy result. The maximum porosity reduced by about 2.6% in 0.16% rGO, compared to the control mix. Unlike the fluorescence microscopy results, the porosity in the G composite reduced by about 1.3% in 0.02% and 0.16% G, compared to the control mix. There is no clear trend noted in the porosity results due to the changes in G dosage in the GCCs. The porosity reduced from 0.01% G to 0.02% G then increased in 0.04% G followed by a gradual reduction in 0.08% G and 0.16% G. This result suggests that the graphene materials densify the composite microstructure bridging the pores as well as filling pores through forming additional content of cement hydration products as indicated in the TGA and XRD quantification results.

3.5.4 DVS pore structure analysis

Fig. 13 shows the DVS sorption isotherms and the pore size distribution of the composites. The maximum water vapour adsorption at 98% RH increased up to 3.4, 1.6 and 3.0% in the GO, rGO and G composites, respectively, compared to the control mix. Larger water adsorption indicates a higher content of C-S-H in the cement paste composite [64]. Fig. 13b, d, and f show the pore size (radius) distribution of the composites in the range of 0.6-22 nm based on the BJH calculation [34]. It could be noted that the intensity of the pores particularly in the range of 0-3 nm radius increased in GO, rGO and G composites, compared to the control mix. This lower range of pores (0-3 nm) is related to the C-S-H and other refined gel pore structures [34]. Therefore, the GCCs have a higher content of C-S-H gel pore structures than the control mix.

Table 6 presents the specific surface area (A_{BET}) and total pore volume (Vm) of the GCCs. The C-S-H gel related to the specific surface area and total pore volume were calculated using the BET method from the DVS sorption isotherms (Fig. 13 a, c, and e). The total pore volume values maximum increased in the GO, rGO and G composite by 4.49, 3.32, and 3.19 $cm^3.g^{-1}$, respectively, compared to the control mix. The specific surface area is similarly influenced as the total pore volume. The 2D nano-plane and functional groups of graphene materials act as nucleation sites during the cement hydration process which increases the cement hydration compounds. In comparison, the active influence of the oxygen-containing functional groups during the cement hydration process results in a slightly higher content of C-S-H in the GO and rGO composites, compared to the G composite. This DVS pore analysis result is in agreement with the findings from TGA, XRD and microstructural image analysis.

The strength enhancement results are not completely consistent with the porosity results. The reason is that graphene materials increase the gel pores, such as C-S-H gel, and decrease the size of larger capillary pores through the formation of ettringite and other secondary hydration products densifying the composite matrix. However, graphene materials also bridge pores and cracks in the composite matrix which may have a minor impact on the porosity but have a considerable impact on the mechanical strength of the composites.

3.6 Transport properties

3.6.1 Electrical resistivity

The electrical resistivity was monitored from the time of demoulding the cube samples after 24 hr of casting to 28 days (Fig. 14). The electrical resistivity gradually increases with the hydration time of the mixes. The electrical resistivity was found to be the highest for the 0.02% GO (approximately 13% higher than the control specimens at 28-day) and gradually decreased with the increasing proportions of GO (Fig. 14a). This was due to the additional hydration and production of cement hydration products such as C-S-H and CH in the nucleation and growth stage which densified the microstructure of the composites. Once again the functional groups of GO together with its non-

electrical conductive property (Table 1) and small plane size 2±1 μm, play an important role in influencing the electrical resistivity of the composite. The resistivity decreases in the rGO composites with the increasing proportions of rGO (Fig. 14b). The greatest reduction of the 28-day electrical resistivity was approximately 18% in the 0.16% rGO composite compared to the control specimens. This uniform reduction of resistivity in the rGO composites was due to higher electrical conductivity (667 S/m) and uniform dispersion of 1-7 μm size of rGO planes, even though rGO increases the cement hydration products due to the presence of a limited amount of functional groups. In the G composite, the resistivity slightly increased up to 0.04% G then gradually decreased with the increasing proportions of G (Fig. 14c). G also influences the cement hydration and at a low concentration level of G (0.01-0.02% G) while the superior electrical conductivity (1000 S/m) may have a minor impact. However, increasing the proportions of G decreases the electrical resistivity due to its high electrical conductivity property.

Overall, the densification of the GCCs microstructure by graphene materials reduces the mean free paths for the electrons transmission which ultimately increased the electrical resistivity in all GO and 0.01-0.02% G composites as similarly reported in [3,34]. Then again, the electrical conductivity property and uniform dispersion of rGO and G have significantly dictated the electrical resistivity of the composites, which is clearly noted in the 28-day resistivity (Fig. 14d).

3.6.2 Water sorptivity

Fig. 15 shows the one-dimensional water sorptivity coefficient of the hardened paste composites specimens at 28 days. The maximum decrease in the sorptivity coefficient was 28% in 0.01% GO, compared to the control specimens, then the sorptivity gradually increased with the increasing proportions of GO in the GCCs. These sorptivity results correspond with the electrical resistivity (Fig. 13a) performance of the GO composites, where resistivity gradually decreased with increasing proportions of GO. This sorptivity performance of GO composite is influenced by the reduction of their workability performance (Fig. 4). Although GO increased C-S-H gel in the composite filling pores, gradual reduction in workability with the increasing proportions of GO may increase entrapped

air void increasing sorptivity results. The maximum sorptivity decreased by about 18% in the 0.16% rGO composite compared to the control specimens. The impact of rGO on cement hydration densified the structure which is reflected in the sorptivity results. Since rGO has a relatively minor impact on the workability, increasing proportions of rGO increase C-S-H gel densifying the matrix and decrease sorptivity. A similar performance is also noted in the G composites. Compared to the control specimens, the sorptivity coefficient maximum decreased by 31% in 0.02% G, 14% in 0.04% G, then again gradually decreased by about 18% and 28% in 0.08% and 0.16% G, respectively. Homogeneous C-S-H gel material with the crystalline hydrated compound formation and strong covalent bond in cement matrix pores by graphene materials may have resulted in this improved sorptivity performance. The pore-filling materials structure may depend on the active functional groups and 2D planes of graphene materials which dictate the type of cement hydration products formation around the nanomaterials. The electrical resistivity and sorptivity results are in agreement with the cement hydration, microstructure characteristics, and strength measurements.

4. Conclusions

This study reported the consistent synthesis of three forms of high-quality graphene materials, GO, rGO and G, from a high-purity epigenetic graphite deposit, and compares their influence in the GCCs at the concentrations of 0.01 to 0.16% by cement weight. The key findings are summarised as follows:

1) Physical strength and the specific characteristics of graphene materials such as oxygen-containing functional groups, plane size, ***d***-spacing, layer thickness, physical properties, and surfactant treatment influence the properties of the GCCs.
2) The workability of composites was reduced gradually with a higher percentage of GO due to its hydrophilic property, while rGO and G have a minor impact on the workability.
3) The oxygen-containing functional groups of GO make it: hydrophilic, efficient to dispersible in water, and lower stack thickness in water, which in turn enhances the cement hydration and reinforces the composite improving the mechanical properties.

4) rGO enhances cement hydration and mechanical properties through reinforcing the composite matrix owing to its reduced amount of functional groups, moderately high physical strength and increased dispersibility in water.
5) The high physical strength, surfactant treatment and an improved dispersibility of G in water reinforce the composite matrix which in turn improved the mechanical properties.
6) Graphene materials influenced the cement hydration process and reinforced the composite microstructure at the nano-micro scale. The functional groups and 2D plane size encourage the CH and C-S-H gel formation during the nucleation and growth stage of the cement hydration process. In the composite matrix, GO has blended well followed by rGO and G within the C-S-H gel materials and cement hydration products.
7) Optical fluorescence and BSE microscopic image analysis, as well as DVS results, indicated that graphene materials effectively reduces the capillary porosity of the composite while the meso and gel pore (< 2 nm) volume associated with C-S-H is slightly increased in the GCCs, compared to the control mix.
8) The electrical conductivity properties of GO, rGO, and G influence the electrical resistivity of the GCCs. A slight increase in the electrical resistivity of GO and 0.01-0.02% G composites is due to the densification of the composite matrix. Although rGO densified the composites, the functional groups and electrical conductivity properties of rGO results in a uniform reduction of the resistivity with increasing proportions of rGO in the GCCs. Similarly, high content G (≥ 0.04%) reduces the resistivity of the composites due to the high electric conductivity of G.
9) The sorptivity coefficient decreased by up to 28% in the 0.1% GO compared to the control specimens, then increased with the increasing proportions of GO in the composites due to the reduction in workability. The sorptivity of rGO and G composite decreased by about 18% and 28% in 0.16% rGO and 0.16% G, respectively, compared to the control specimen, regardless of their decreased electrical resistivity values. This is due to the influence of rGO and G in the densification of the composite microstructure through the cement hydration and pore refinement.

Future research is required to investigate the performance of graphene materials in more complex GCCs systems such as mortar and concrete as well as their long-term durability performance. The influence of rGO and G in achieving self-sensing abilities in the GCCs could be further investigated.

Acknowledgements

The authors are grateful for support from Professor Panesar's NSERCNatural Sciences and Engineering Research Council of Canada (NSERC) Discovery Grant, University of Toronto- Dean's Strategic Fund, and her Erwin Edward Hart Early Career Award. The authors are thankful to ZEN Graphene Solutions for their contribution of the purified graphite and graphene materials supply. The authors are also grateful to Professor Aicheng Chen of the Department of Chemistry, the University of Guelph for his contribution to GO and rGO synthesis, and Professor Giovanni Fanchini of the Department of Physics and Astronomy, Western University for his contribution in G synthesis.

Appendix-A

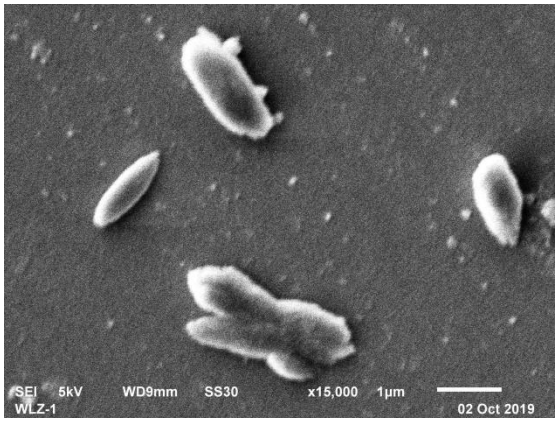

(a)

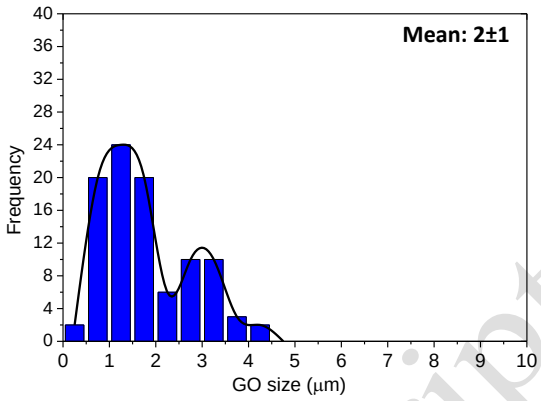

(b)

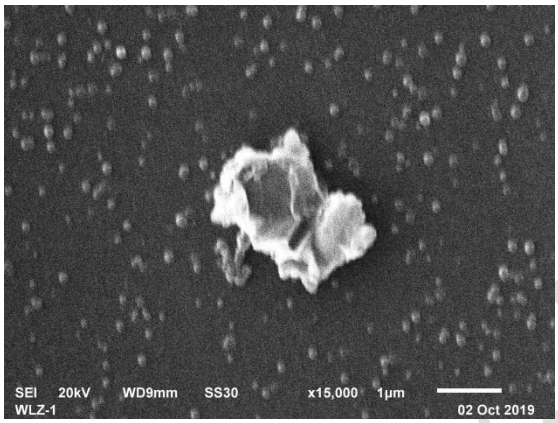

(c)

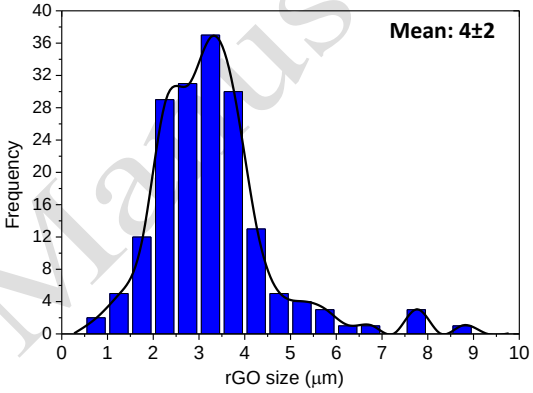

(d)

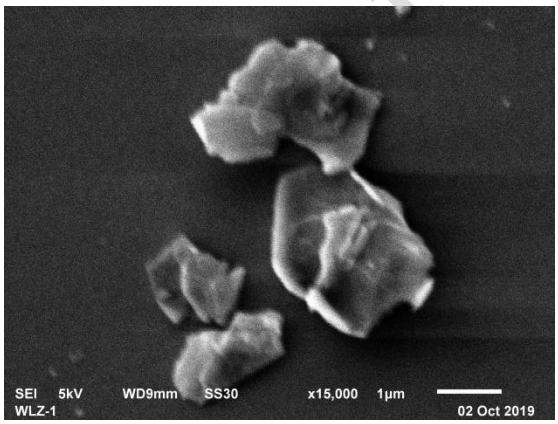

(e)

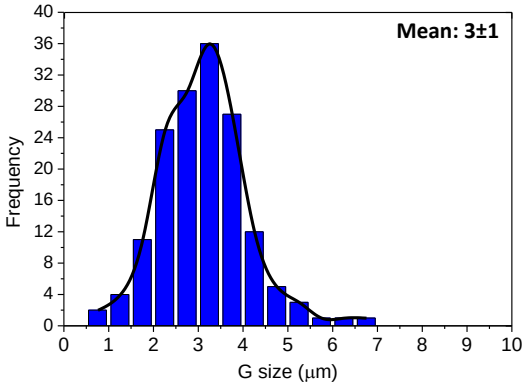

(f)

Fig. A1. Plane size distribution from SEM image analysis, (a) typical SEM image of GO, (b) particle size distribution of GO, (c) typical image of rGO, (d) particle size distribution of rGO, (e) typical image of G, and (f) particle size distribution of G.

Appendix-B Supplementary data

Supplementary data to this article can be found online at https://doi.org/10.1016/j.compositesb.2020.108063.

References

[1] Novoselov KS, Geim AK, Morozov S V., Jiang D, Zhang Y, Dubonos S V., et al. Electric field effect in atomically thin carbon films. Science (80-) 2004;306:666–9.

[2] Cong H-P, Ren X-C, Wang P, Yu S-H. Flexible graphene–polyaniline composite paper for high-performance supercapacitor. Energy Environ Sci 2013;6:1185. doi:10.1039/c2ee24203f.

[3] Qureshi TS, Panesar DK, Sidhureddy B, Chen A, Wood PC. Nano-cement composite with graphene oxide produced from epigenetic graphite deposit. Compos Part B Eng 2019;159:248–58. doi:10.1016/j.compositesb.2018.09.095.

[4] Gholampour A, Valizadeh Kiamahalleh M, Tran DNH, Ozbakkaloglu T, Losic D. From Graphene Oxide to Reduced Graphene Oxide: Impact on the Physiochemical and Mechanical Properties of Graphene–Cement Composites. ACS Appl Mater Interfaces 2017:acsami.7b16736. doi:10.1021/acsami.7b16736.

[5] Arvidsson R, Kushnir D, Sandén BA, Molander S. Prospective Life Cycle Assessment of Graphene Production by Ultrasonication and Chemical Reduction. Environ Sci Technol 2014;48:4529–36. doi:10.1021/es405338k.

[6] León V, Quintana M, Herrero MA, Fierro JLG, Hoz AD La, Prato M, et al. Few-layer graphenes from ball-milling of graphite with melamine. Chem Commun 2011;47:10936–8. doi:10.1039/c1cc14595a.

[7] Compton OC, Nguyen ST. Graphene Oxide, Highly Reduced Graphene Oxide, and Graphene: Versatile Building Blocks for Carbon-Based Materials. Small 2010;6:711–23. doi:10.1002/smll.200901934.

[8] Qureshi TS, Panesar DK. A comparison of graphene oxide, reduced graphene oxide and pure graphene: early age properties of cement composites. 2nd RILEM Spring Conv. Int. Conf. Sustain. Mater. Syst. Struct., Rovinj, Croatia: 2019.

[9] Lv W, Li Z, Deng Y, Yang Q-H, Kang F. Graphene-based materials for electrochemical energy storage devices: Opportunities and challenges. Energy Storage Mater 2016;2:107–38. doi:10.1016/j.ensm.2015.10.002.

[10] Zhu Y, Murali S, Cai W, Li X, Suk JW, Potts JR, et al. Graphene and Graphene Oxide: Synthesis, Properties, and Applications. Adv Mater 2010;22:3906–24. doi:10.1002/adma.201001068.

[11] Chuah S, Pan Z, Sanjayan JG, Wang CM, Duan WH. Nano reinforced cement and concrete composites and new perspective from graphene oxide. Constr Build Mater 2014;73:113–24. doi:10.1016/j.conbuildmat.2014.09.040.

[12] Chu H, Jiang J, Sun W, Zhang M. Effects of graphene sulfonate nanosheets on mechanical and thermal properties of sacrificial concrete during high temperature exposure. Cem Concr Compos 2017;82:252–64. doi:10.1016/j.cemconcomp.2017.06.007.

[13] Qureshi TS, Panesar DK. A review: the effect of graphene oxide on the properties of cement-based composites. CSCE Annu. Conf., Vancouver, Canada: 2017, p. 642–1 to 642–10.

[14] Birenboim M, Nadiv R, Alatawna A, Buzaglo M, Schahar G, Lee J, et al. Reinforcement and workability aspects of graphene-oxide-reinforced cement nanocomposites. Compos Part B Eng 2019;161:68–76. doi:10.1016/J.COMPOSITESB.2018.10.030.

[15] Yang H, Cui H, Tang W, Li Z, Han N, Xing F. A critical review on research progress of graphene/cement based composites. Compos Part A Appl Sci Manuf 2017;102:273–96. doi:10.1016/j.compositesa.2017.07.019.

[16] Mokhtar MM, Abo-El-Enein SA, Hassaan MY, Morsy MS, Khalil MH. Mechanical performance, pore structure and micro-structural characteristics of graphene oxide nano platelets reinforced cement. Constr Build Mater 2017;138:333–9. doi:10.1016/j.conbuildmat.2017.02.021.

[17] Li W, Li X, Chen SJ, Liu YM, Duan WH, Shah SP. Effects of graphene oxide on early-age hydration and electrical resistivity of Portland cement paste. Constr Build Mater 2017;136:506–14. doi:10.1016/j.conbuildmat.2017.01.066.

[18] Qiu C, Zhou Q, Lv S, Ma Y. Regulation of GO on cement hydration crystals and its toughening effect. Mag Concr Res 2013;65:1246–54. doi:10.1680/macr.13.00190.

[19] Saafi M, Tang L, Fung J, Rahman M, Liggat J. Enhanced properties of graphene/fly ash geopolymeric composite cement. Cem Concr Res 2015;67:292–9. doi:10.1016/j.cemconres.2014.08.011.

[20] Murugan M, Santhanam M, Sen Gupta S, Pradeep T, Shah SP. Influence of 2D rGO nanosheets on the properties of OPC paste. Cem Concr Compos 2016;70:48–59. doi:10.1016/j.cemconcomp.2016.03.005.

[21] Li X, Lu Z, Chuah S, Li W, Liu Y, Duan WH, et al. Effects of graphene oxide aggregates on hydration degree, sorptivity, and tensile splitting strength of cement paste. Compos Part A Appl Sci Manuf 2017;100:1–8. doi:10.1016/J.COMPOSITESA.2017.05.002.

[22] Sun S, Ding S, Han B, Dong S, Yu X, Zhou D, et al. Multi-layer graphene-engineered cementitious composites with multifunctionality/intelligence. Compos Part B Eng 2017;129:221–32. doi:10.1016/j.compositesb.2017.07.063.

[23] Mohammed A, Sanjayan JG, Duan WH, Nazari A. Incorporating graphene oxide in cement composites: A study of transport properties. Constr Build Mater 2015;84:341–7. doi:10.1016/j.conbuildmat.2015.01.083.

[24] Pan Z, He L, Qiu L, Korayem AH, Li G, Zhu JW, et al. Mechanical properties and microstructure of a graphene oxide–cement composite. Cem Concr Compos 2015;58:140–7. doi:10.1016/j.cemconcomp.2015.02.001.

[25] Horszczaruk E, Mijowska E, Kalenczuk RJ, Aleksandrzak M, Mijowska S. Nanocomposite of cement/graphene oxide - Impact on hydration kinetics and Young's modulus. Constr Build Mater 2015;78:234–42. doi:10.1016/j.conbuildmat.2014.12.009.

[26] Wang Q, Wang J, Lu C, Liu B, Zhang K, Li C. Influence of graphene oxide additions on the microstructure and mechanical strength of cement. New Carbon Mater 2015;30:349–56. doi:10.1016/S1872-5805(15)60194-9.

[27] Lv S, Ma Y, Qiu C, Sun T, Liu J, Zhou Q. Effect of graphene oxide nanosheets of microstructure and mechanical properties of cement composites. Constr Build Mater 2013;49:121–7. doi:10.1016/j.conbuildmat.2013.08.022.

[28] Gong K, Pan Z, Korayem AH, Qiu L, Li D, Collins F, et al. Reinforcing Effects of Graphene Oxide on Portland Cement Paste. J Mater Civ Eng 2015;27:A4014010. doi:10.1061/(ASCE)MT.1943-5533.0001125.

[29] An J, Nam BH, Alharbi Y, Cho BH, Khawaji M. Edge-oxidized graphene oxide (EOGO) in cement composites: Cement hydration and microstructure. Compos Part B Eng 2019;173:106795. doi:10.1016/J.COMPOSITESB.2019.05.006.

[30] Cui H, Yan X, Tang L, Xing F. Possible pitfall in sample preparation for SEM analysis - A discussion of the paper "Fabrication of polycarboxylate/graphene oxide nanosheet composites by copolymerization for reinforcing and toughening cement composites" by Lv et al. Cem Concr Compos 2017;77:81–5. doi:10.1016/j.cemconcomp.2016.12.007.

[31] Zhao L, Guo X, Ge C, Li Q, Guo L, Shu X, et al. Mechanical behavior and toughening mechanism of polycarboxylate superplasticizer modified graphene oxide reinforced cement composites. Compos Part B Eng 2017;113:308–16. doi:10.1016/j.compositesb.2017.01.056.

[32] Chen ZS, Zhou X, Wang X, Guo P. Mechanical behavior of multilayer GO carbon-fiber cement composites. Constr Build Mater 2018;159:205–12. doi:10.1016/j.conbuildmat.2017.10.094.

[33] Li X, Liu YM, Li WG, Li CY, Sanjayan JG, Duan WH, et al. Effects of graphene oxide agglomerates on workability, hydration, microstructure and compressive strength of cement paste. Constr Build Mater 2017;145:402–10. doi:10.1016/J.CONBUILDMAT.2017.04.058.

[34] Qureshi TS, Panesar DK. Impact of graphene oxide and highly reduced graphene oxide on cement based composites. Constr Build Mater 2019;206:71–83. doi:10.1016/j.conbuildmat.2019.01.176.

[35] Li G, Yuan JB, Zhang YH, Zhang N, Liew KM. Microstructure and mechanical performance of graphene reinforced cementitious composites. Compos Part A Appl Sci Manuf 2018;114:188–95. doi:10.1016/J.COMPOSITESA.2018.08.026.

[36] Li G, Zhang LW. Microstructure and phase transformation of graphene-cement composites under high temperature. Compos Part B Eng 2019;166:86–94. doi:10.1016/J.COMPOSITESB.2018.11.127.

[37] Dela Vega MSDC, Vasquez MR. Plasma-functionalized exfoliated multilayered graphene as cement reinforcement. Compos Part B Eng 2019;160:573–85. doi:10.1016/J.COMPOSITESB.2018.12.055.

[38] Marcano DC, Kosynkin D V., Berlin JM, Sinitskii A, Sun Z, Slesarev A, et al. Improved Synthesis of Graphene Oxide. ACS Nano 2010;4:4806–14. doi:10.1021/nn1006368.

[39] Boopathi S, Narayanan TN, Senthil Kumar S. Improved heterogeneous electron transfer kinetics of fluorinated graphene derivatives. Nanoscale 2014;6:10140–6. doi:10.1039/c4nr02563f.

[40] Seo J-WT, Green AA, Antaris AL, Hersam MC. High-Concentration Aqueous Dispersions of Graphene Using Nonionic, Biocompatible Block Copolymers. J Phys Chem Lett 2011;2:1004–8. doi:10.1021/jz2003556.

[41] Van Middelkoop S, Cen A, Bauld R, Fanchini G. In-line chemiresistors based on multilayer graphene for cadmium dication sensing in water. FlatChem 2019;17. doi:10.1016/j.flatc.2019.100118.

[42] Collins F, Lambert J, Duan WH. The influences of admixtures on the dispersion, workability, and strength of carbon nanotube-OPC paste mixtures. Cem Concr Compos 2012;34:201–7. doi:10.1016/j.cemconcomp.2011.09.013.

[43] ASTM Standard C1437-07. Standard Test Method for Flow of Hydraulic Cement Mortar. 2007. doi:10.1520/C1437-07.

[44] ASTM C109 / C109M-16a. Standard Test Method for Compressive Strength of Hydraulic Cement Mortars (Using 2-in. or [50-mm] Cube Specimens). 2016. doi:10.1520/C0109_C0109M-16A.

[45] ASTM C348-14. Standard Test Method for Flexural Strength of Hydraulic-Cement Mortars. 2014. doi:10.1520/C0348-14.

[46] Qureshi TS, Panesar DK, Peterson K. Thin section microscopy and DVS study to determine the influence of graphene materials on the microstructure of cement based composite. 17th Euroseminar Microsc. Appl. to Build. Mater., 2019, p. 134–40.

[47] Panesar DK, Francis J. Influence of limestone and slag on the pore structure of cement paste based on mercury intrusion porosimetry and water vapour sorption measurements. Constr Build Mater 2014;52:52–8. doi:10.1016/J.CONBUILDMAT.2013.11.022.

[48] Layssi H, Ghods P, Alizadeh AR, Salehi M. Electrical resistivity of concrete. Concr Int 2015;37:41–6.

[49] Sengul O. Use of electrical resistivity as an indicator for durability. Constr Build Mater 2014;73:434–41. doi:10.1016/j.conbuildmat.2014.09.077.

[50] Qureshi TS, Al-Tabbaa a. Self-healing of drying shrinkage cracks in cement-based materials incorporating reactive MgO. Smart Mater Struct 2016;25:084004. doi:10.1088/0964-1726/25/8/084004.

[51] Mishra SK, Tripathi SN, Choudhary V, Gupta BD. SPR based fibre optic ammonia gas sensor utilizing nanocomposite film of PMMA/reduced graphene oxide prepared by in situ polymerization. Sensors Actuators, B Chem 2014;199:190–200. doi:10.1016/j.snb.2014.03.109.

[52] Chen C, Long M, Xia M, Zhang C, Cai W. Reduction of graphene oxide by an in-situ photoelectrochemical method in a dye-sensitized solar cell assembly. Nanoscale Res Lett 2012;7:101. doi:10.1186/1556-276X-7-101.

[53] Ferrari AC, Meyer JC, Scardaci V, Casiraghi C, Lazzeri M, Mauri F, et al. Raman Spectrum of Graphene and Graphene Layers. Phys Rev Lett 2006;97:187401. doi:10.1103/PhysRevLett.97.187401.

[54] Korucu H, Şimşek B, Uygunoğlu T, Güvenç AB, Yartaşı A. Statistical approach to carbon based materials reinforced cementitious composites: Mechanical, thermal, electrical and sulfuric acid resistance properties. Compos Part B Eng 2019;171:347–60. doi:10.1016/J.COMPOSITESB.2019.05.017.

[55] Saafi M, Tang L, Fung J, Rahman M, Sillars F, Liggat J, et al. Graphene/fly ash geopolymeric composites as self-sensing structural materials. Smart Mater Struct 2014;23:065006. doi:10.1088/0964-1726/23/6/065006.

[56] Al-Dahawi A, Sarwary MH, Öztürk O, Yıldırım G, Akın A, Şahmaran M, et al. Electrical percolation threshold of cementitious composites possessing self-sensing functionality incorporating different carbon-based materials. Smart Mater Struct 2016;25:105005. doi:10.1088/0964-1726/25/10/105005.

[57] Zhao D, Chen J, Gao Q, Ge HY. Graphene Oxide/Cement Composites for Electromagnetic Interference Shielding. Mater Sci Forum 2014;809-810:485–9. doi:10.4028/www.scientific.net/MSF.809-810.485.

[58] Yang H, Monasterio M, Cui H, Han N. Experimental study of the effects of graphene oxide on microstructure and properties of cement paste composite. Compos Part A Appl Sci Manuf 2017;102:263–72. doi:10.1016/j.compositesa.2017.07.022.

[59] Roychand R, De Silva S, Law D, Setunge S. High volume fly ash cement composite modified with nano silica, hydrated lime and set accelerator. Mater Struct 2016;49:1997–2008. doi:10.1617/s11527-015-0629-z.

[60] Schöler A, Lothenbach B, Winnefeld F, Zajac M. Hydration of quaternary Portland cement blends containing blast-furnace slag, siliceous fly ash and limestone powder. Cem Concr Compos 2015;55:374–82. doi:10.1016/j.cemconcomp.2014.10.001.

[61] Li X, Korayem AH, Li C, Liu Y, He H, Sanjayan JG, et al. Incorporation of graphene oxide and silica fume into cement paste: A study of dispersion and compressive strength. Constr Build Mater 2016;123:327–35. doi:10.1016/j.conbuildmat.2016.07.022.

[62] Wong HS, Head MK, Buenfeld NR. Pore segmentation of cement-based materials from backscattered electron images. Cem Concr Res 2006;36:1083–90. doi:10.1016/J.CEMCONRES.2005.10.006.

[63] Scrivener KL, Patel H, Pratt PL, Parrott LJ, Struble LJ, Brown PW. Microstructural Development During Hydration of Cement. Mater Res Soc 1987;85:39.

[64] Baroghel-Bouny V. Water vapour sorption experiments on hardened cementitious materials: Part I: Essential tool for analysis of hygral behaviour and its relation to pore structure. Cem Concr Res 2007;37:414–37. doi:10.1016/J.CEMCONRES.2006.11.019.

List of Tables

Tables

Table 1: Physical properties of graphene materials [8].

Physical properties	GO- Graphene oxide	rGO- Reduced graphene oxide	G- Pristine graphene
Tensile strength	~0.13 GPa*	unknown	~130 GPa*
Elastic modulus	23-42 GPa*	250±150 GPa**	1000 GPa*
Elongation at break	0.6 %*	unknown	0.8%*
Electrical conductivity	Non conductive	~667 S/m***	~1000 S/m
Dispersibility in water	Highly dispersible	Moderately dispersible	Not dispersible

Note: * Reference [9,11], ** Reference [10], ***Measured in a 20 nm thickness film.

Table 2. The chemical composition of general use cement in percentage.

SiO_2	Al_2O_3	Fe_2O_3	CaO	MgO	SO_3	Total Alkali	Free Lime	LOI
19.3	5.50	2.70	61.20	2.60	4.00	0.92	0.60	2.50

Table 3. pH of graphene dispersed water.

Graphene materials	wt% of cement				
	0.01%	0.02%	0.04%	0.08%	0.16%
GO	3.72	3.74	3.48	3.28	3.03
rGO	9.09	9.61	9.98	10.03	10.24
G	6.96	6.92	6.77	6.2	6.09

Table 4. Mix proportions of the graphene-cement composites.

Mix	GO (wt.% of Cement)	rGO (wt.% of Cement)	Graphene (G) (wt.% of Cement)	Cement (g)	Water (g)
Control	0	0	0	3000	1350
0.01% GO	0.01	0	0	3000	1350
0.02% GO	0.02	0	0	3000	1350
0.04% GO	0.04	0	0	3000	1350
0.08% GO	0.08	0	0	3000	1350
0.16% GO	0.16	0	0	3000	1350
0.01% rGO	0	0.01	0	3000	1350
0.02% rGO	0	0.02	0	3000	1350
0.04% rGO	0	0.04	0	3000	1350
0.08% rGO	0	0.08	0	3000	1350
0.16% rGO	0	0.16	0	3000	1350
0.01% G	0	0	0.01	3000	1350
0.02% G	0	0	0.02	3000	1350
0.04% G	0	0	0.04	3000	1350
0.08% G	0	0	0.08	3000	1350
0.16% G	0	0	0.16	3000	1350

Table 5. Summary of GO, rGO and G characterization.

	GO	rGO	G
Chemical structure	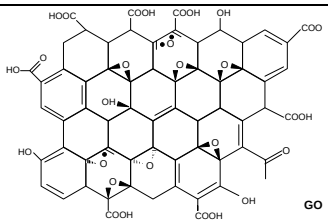	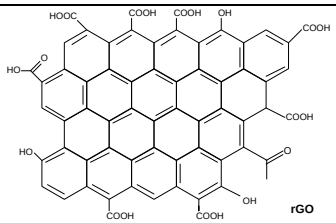	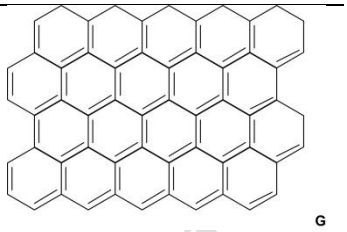
C, O Element (%)	C (62-65%) O (35-38%)	C (77-87%) O (13-22%)	C (99%) O (--)
Functional groups	-COOH, -OH, C-O-C, C=O	-COOH, -OH, C=O	Not applicable
Affinity for water	Hydrophilic	Moderately hydrophilic	Hydrophobic
Raman (I_D/I_G) ratio	0.83	0.96	0.25
Crystallite size [1]	20.64 nm	18.28 nm	70.20 nm
d spacing [2]	0.85 nm	0.35	0.33 nm
Plane size [3]	2±1 µm	4±2 µm	3±1 µm
Layer thickness [4]	1.0 nm	1.2 nm	1.4 nm
Number of layers [5]	1-3	1-3	3-5
Stack thickness in water dispersion [6]	1-1.7 nm	125-175 nm	180-230 nm

[1] Measured from Raman (I_D/I_G) ratio using the relation described in [3]
[2] Measured from XRD
[3] Measured from SEM image analysis
[4] Typical layer thickness measured from AFM image analysis
[5] Measured from the AFM layer thickness divided by XRD single layer thickness
[6] Occasional stack of layers noted in AFM due to agglomeration after dispersed in water

Table 6. Specific surface area and total pore volume in the GCCs for the range of pore diameter from 0 to 22 nm.

	Control	0.01% GO	0.02% GO	0.04% GO	0.08% GO	0.16% GO
Specific surface area ($m^2.g^{-1}$), A_{BET}	60.45	67.93	67.41	69.31	73.11	71.88
Total pore volume, Vm ($cm^3.g^{-1}$)	21.42	24.08	23.89	24.57	25.91	25.48
		0.01% rGO	0.02% rGO	0.04% rGO	0.08% rGO	0.16% rGO
Specific surface area ($m^2.g^{-1}$), A_{BET}		63.35	68.68	68.56	69.80	69.25
Total pore volume, Vm ($cm^3.g^{-1}$)		22.45	24.34	24.65	24.74	24.55
		0.01% G	0.02% G	0.04% G	0.08% G	0.16% G
Specific surface area ($m^2.g^{-1}$), A_{BET}		58.39	67.16	64.10	68.54	69.28
Total pore volume, Vm ($cm^3.g^{-1}$)		20.70	23.80	22.72	24.61	24.54

List of Figures

Fig. 12 Porosity of the composites from BSE images using tangent-slope thresholding method and overflow segmentation method, (a) typical BSE image of the GCCs (0.16% rGO), (b) cumulative greyscale histogram of BSE image 0.16% rGO and application of tangent-slope thresholding method, (c) pores segmented (black pixel) from 0.16% rGO at threshold level 86 indicating porosity of paste = 11.72%, and (d) average porosity of paste.

Fig. 13 DVS analysis results: (a) GO composite adsorption and desorption, (b) GO composite pore volume distribution, (c) rGO composite adsorption and desorption, (d) rGO composite pore volume distribution, (e) G composite adsorption and desorption, and (f) G composite pore volume distribution.

Fig. 14 Evolution of electrical resistivity, (a) GO composite, (b) rGO composite, (c) G composite, and (d) average electrical resistivity at 28-day GCCs.

Fig. 15 Water sorptivity coefficient of 28-day GCCs.

Figures

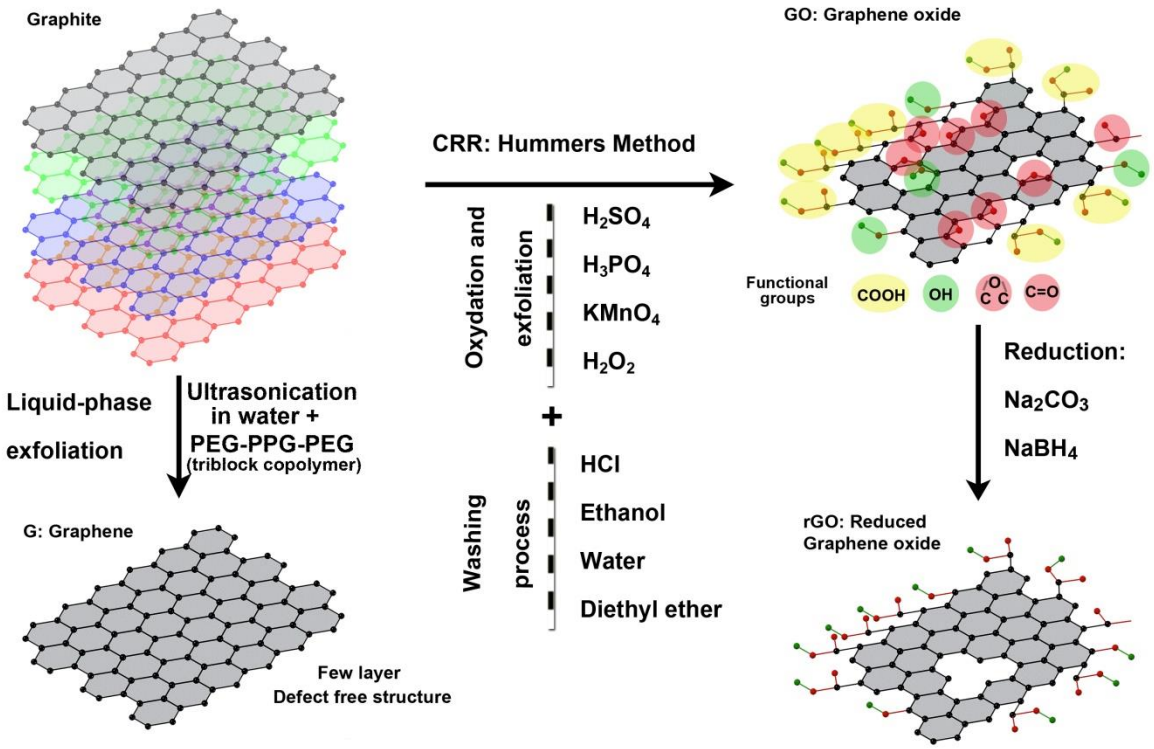

Fig. 1 Production of graphene materials (GO, rGO, and G) from graphite.

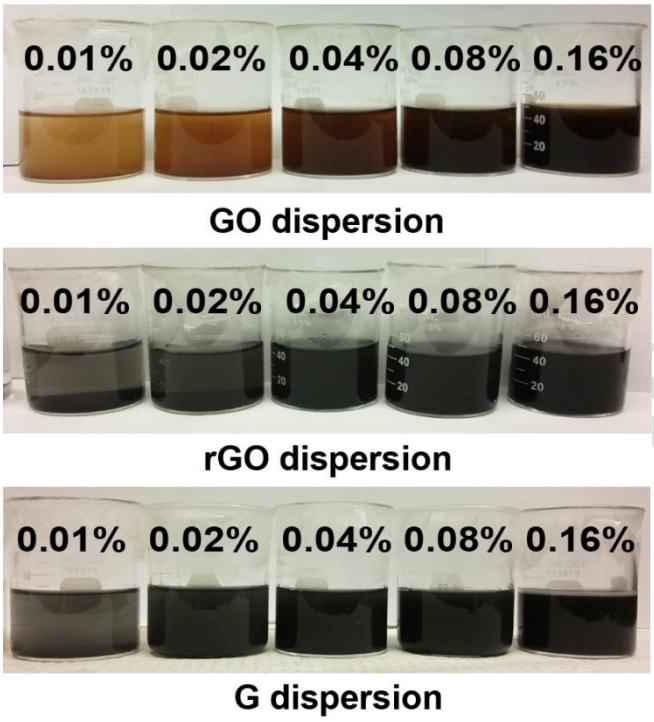

Fig. 2 Graphene solutions after dispersion in water.

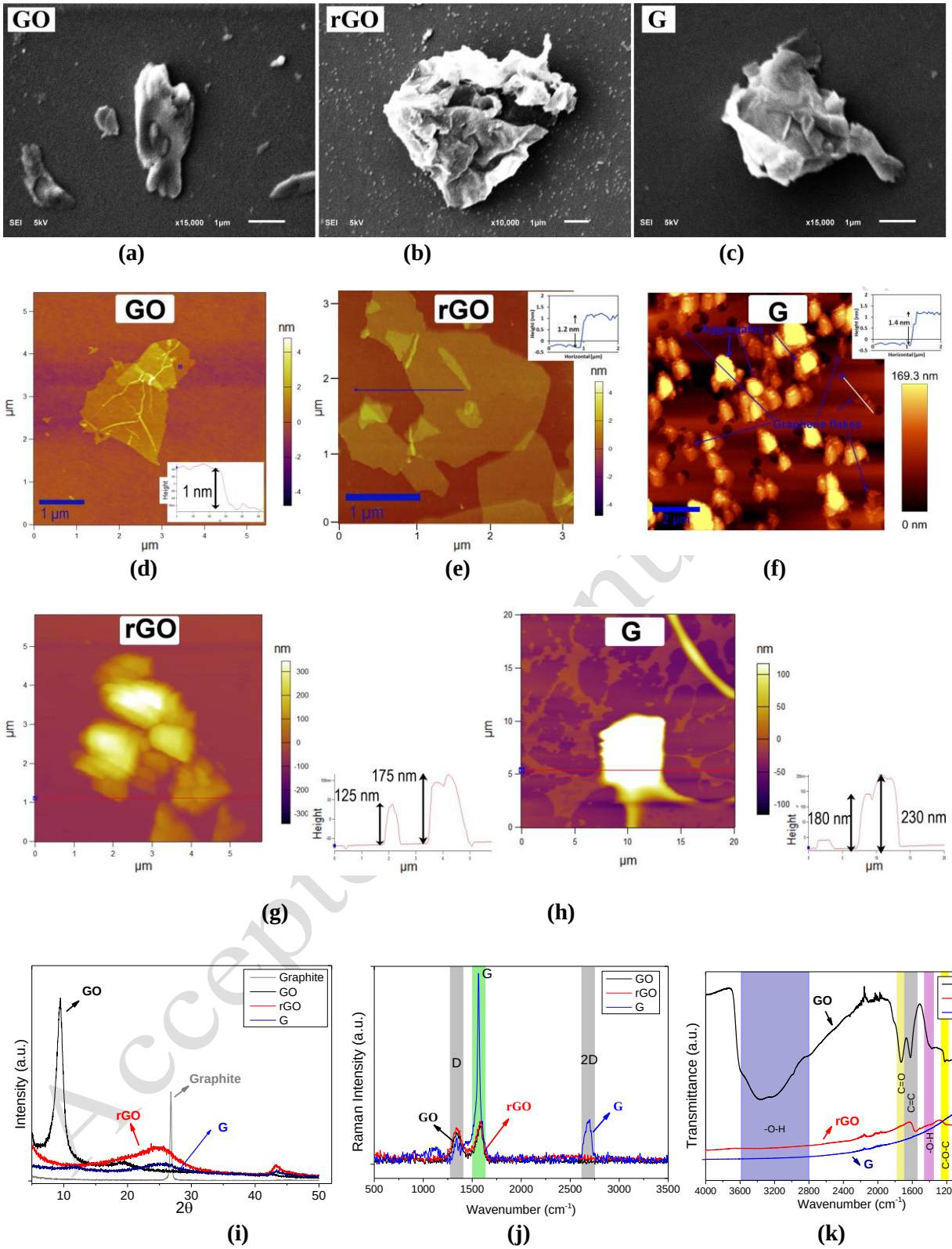

Fig. 3 Characterisation of graphene materials; SEM images: (a) GO, (b) rGO, and (c) G; typical AFM images in water dispersion: (d) GO, (e) rGO, and (f) G; occetional AFM images for stackness in water dispersion: (g) rGO and (h) G; (i) XRD pattern, (j) Raman spectroscopy, and (k) FTIR graph.

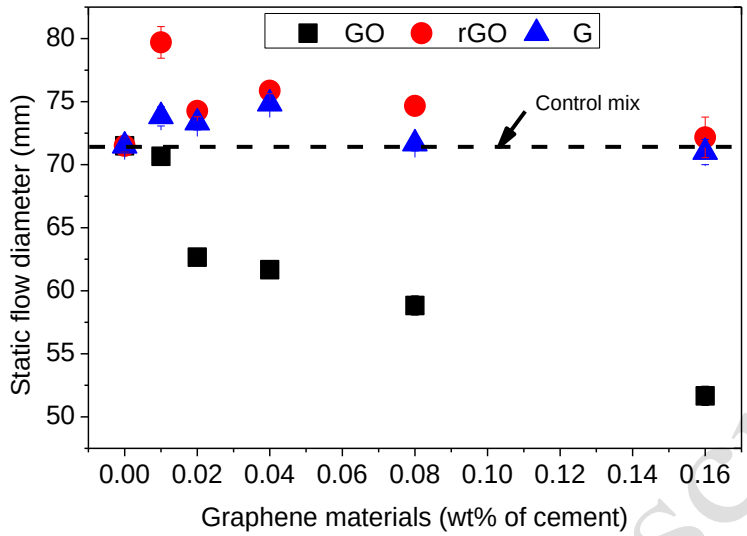

(a)

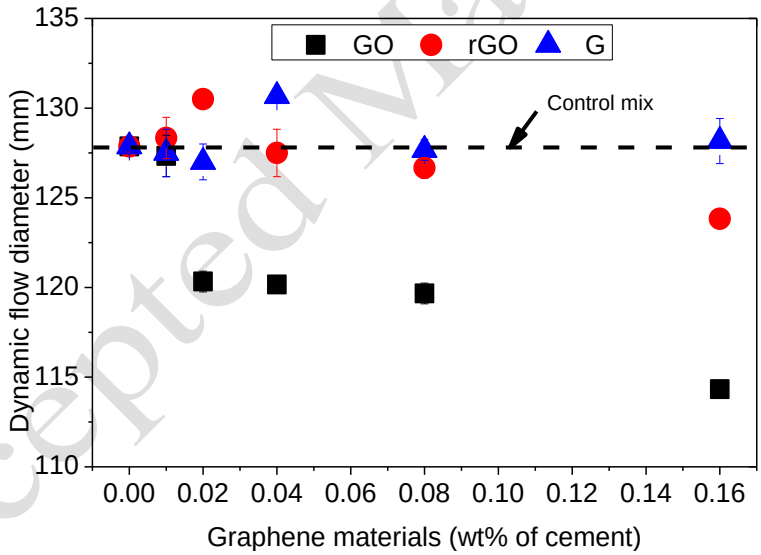

(b)

Fig. 4 Flow diameter in mini-slump test, (a) Static flow, and (b) Dynamic flow [8].

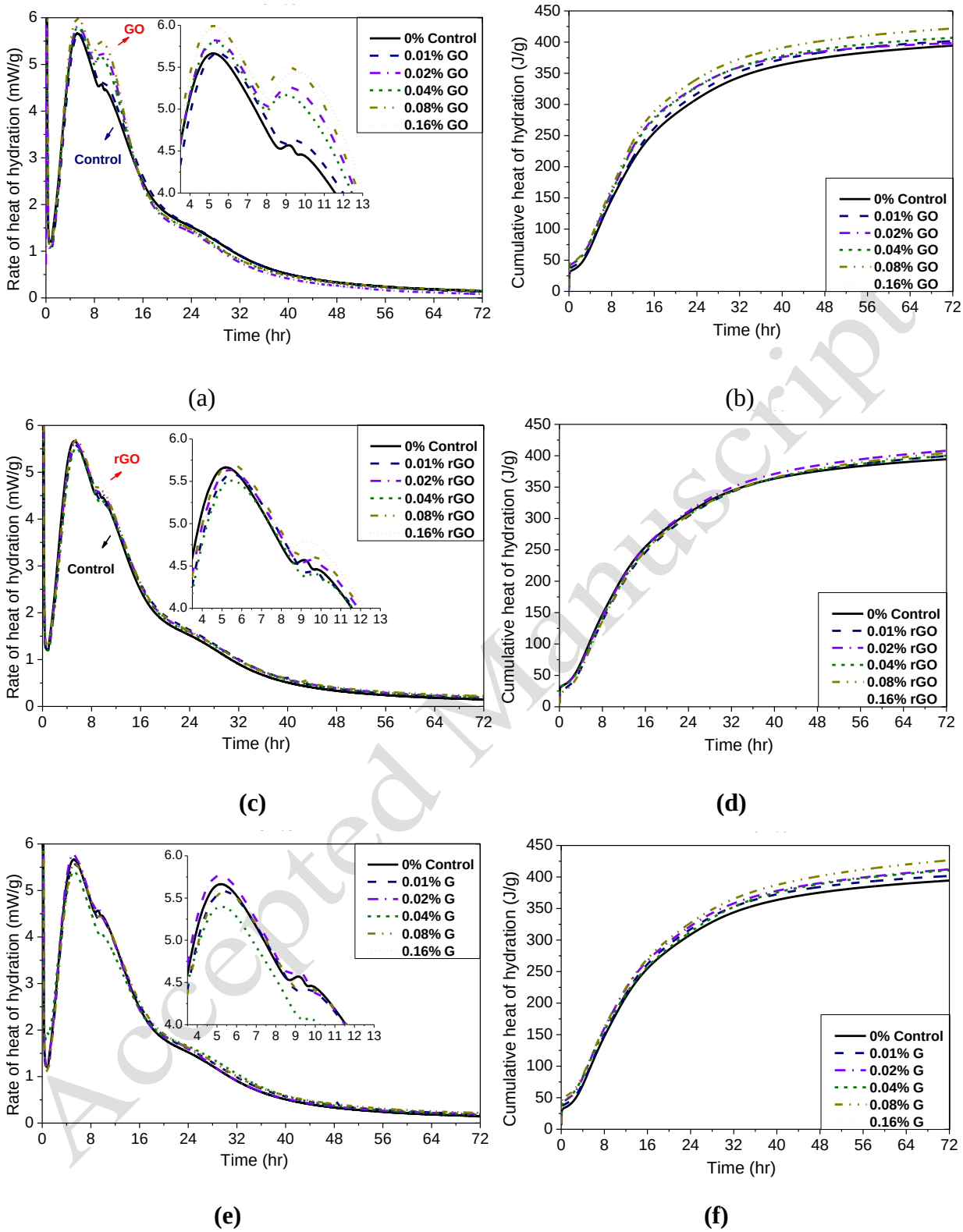

Fig. 5 Hydration heat release of composite pastes during first 72 h hydration: (a) GO composites rate of heat of hydration, (b) GO composites cumulative heat of hydration, (c) rGO composites rate of heat of hydration, (d) rGO composites cumulative heat of hydration, (e) G composites rate of heat of hydration, and (f) G composites cumulative heat of hydration.

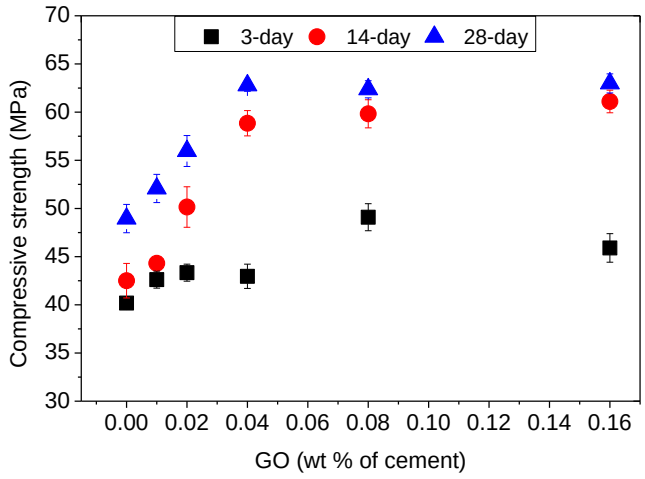

(a)

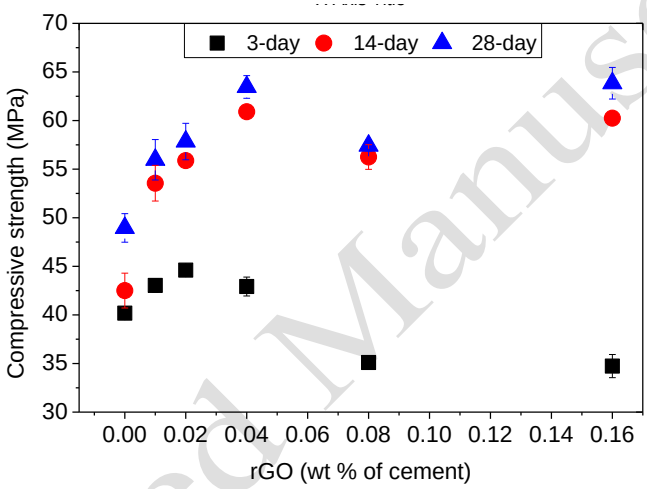

(b)

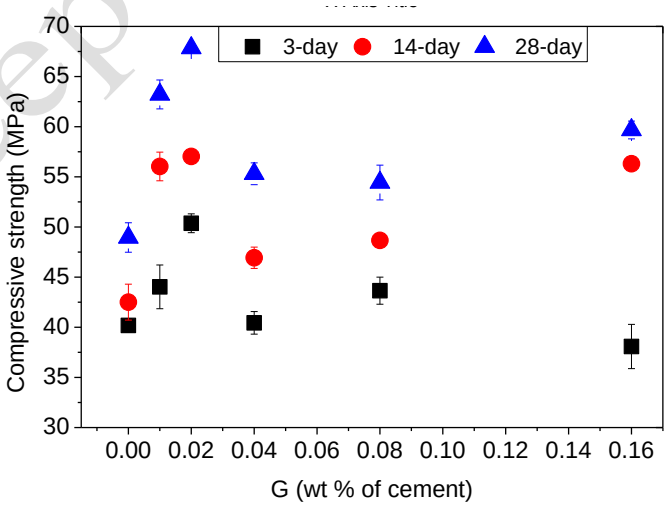

(c)

Fig. 6 Compressive strength, (a) GO composites, (b) rGO composites, and (c) G composites.

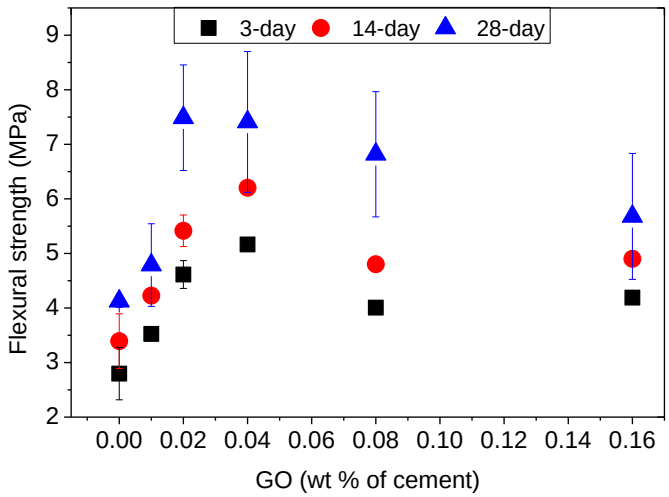

(a)

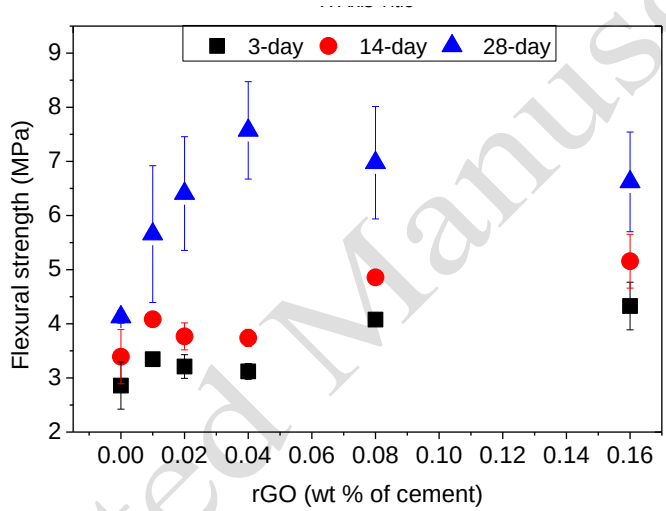

(b)

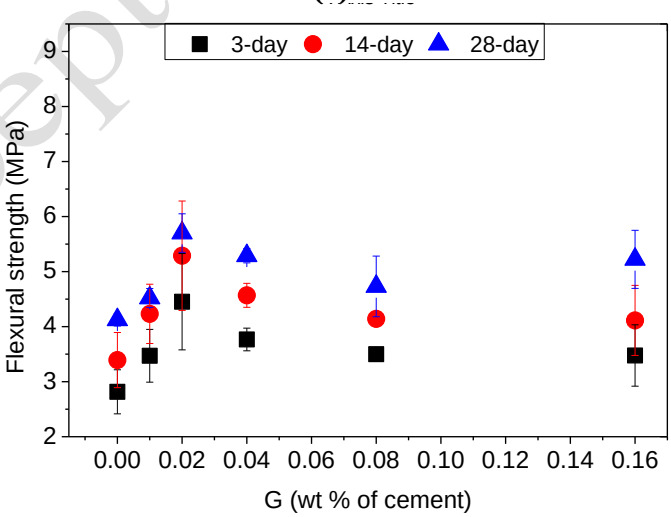

(c)

Fig. 7 Flexural strength, (a) GO composites, (b) rGO composites, and (c) G composites.

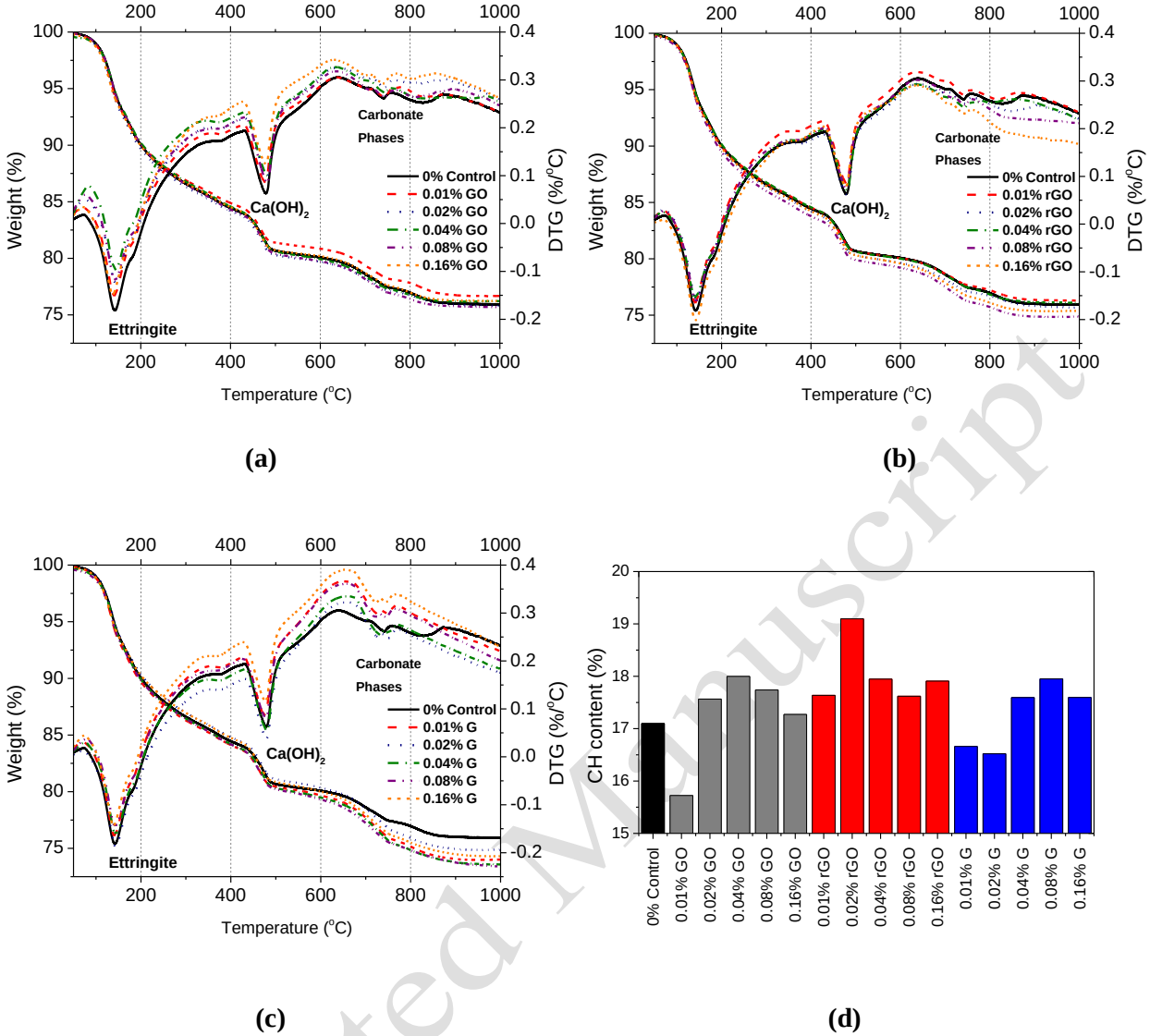

(a) **(b)**

(c) **(d)**

Fig. 8 Thermogravimetric analysis on 28-day composites: (a) TGA and DTG curves of GO composites, (b) TGA and DTG curves of rGO composites , (c) TGA and DTG curves of G composites, and (d) CH content in percentage.

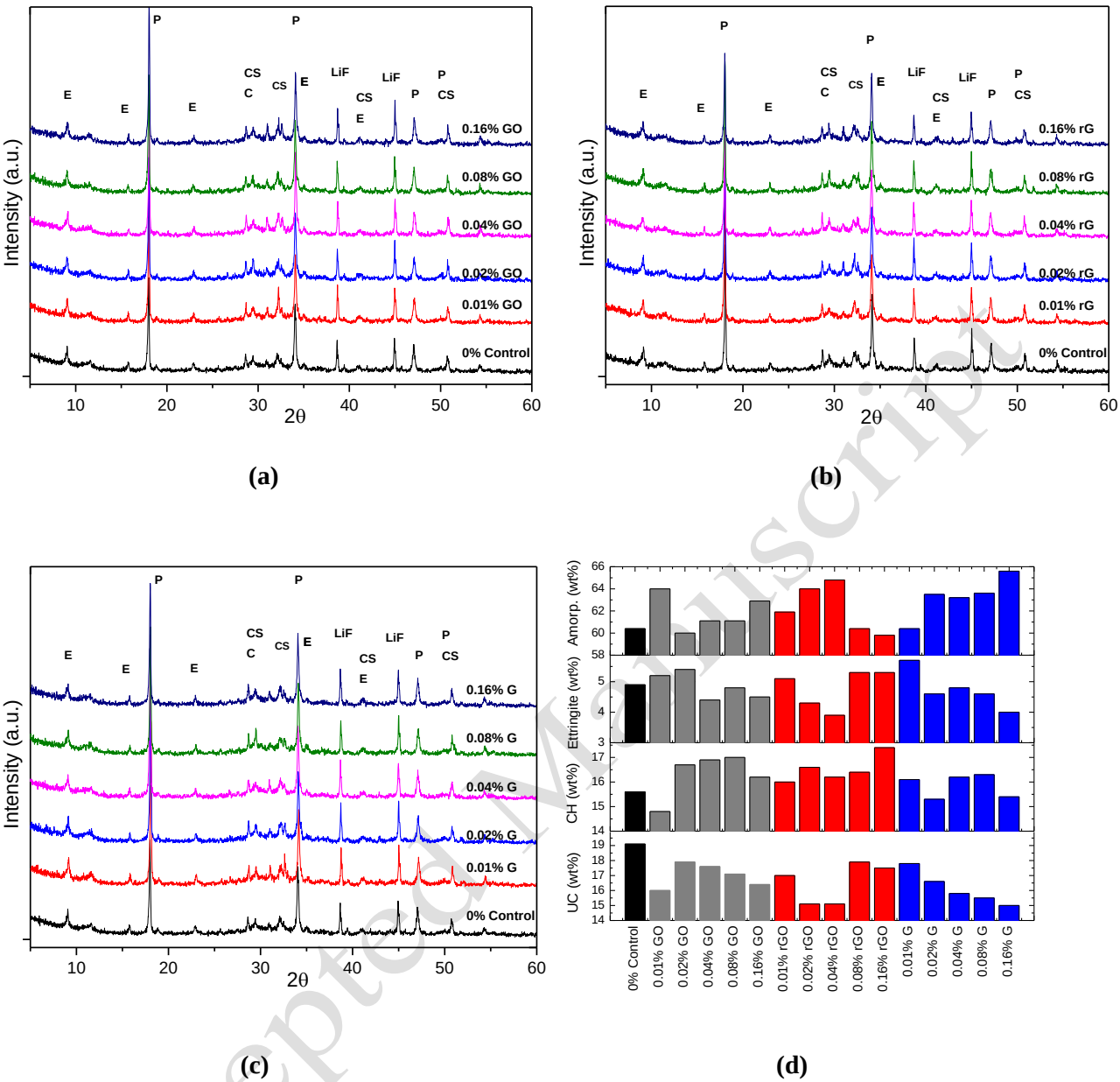

(a) **(b)**

(c) **(d)**

Fig. 9 XRD curves of 28-day hydrated composites: (a) GO composites, (b) rGO composites, (c) G composite. (Graph notations: E= Ettringite, C= Calcite, CS= C_2S and C_3S, P= Portlandite (CH), LiF= Lithium fluoride), and (d) theoretical volume estimated by Rietveld quantification method (UC = unreacted cement).

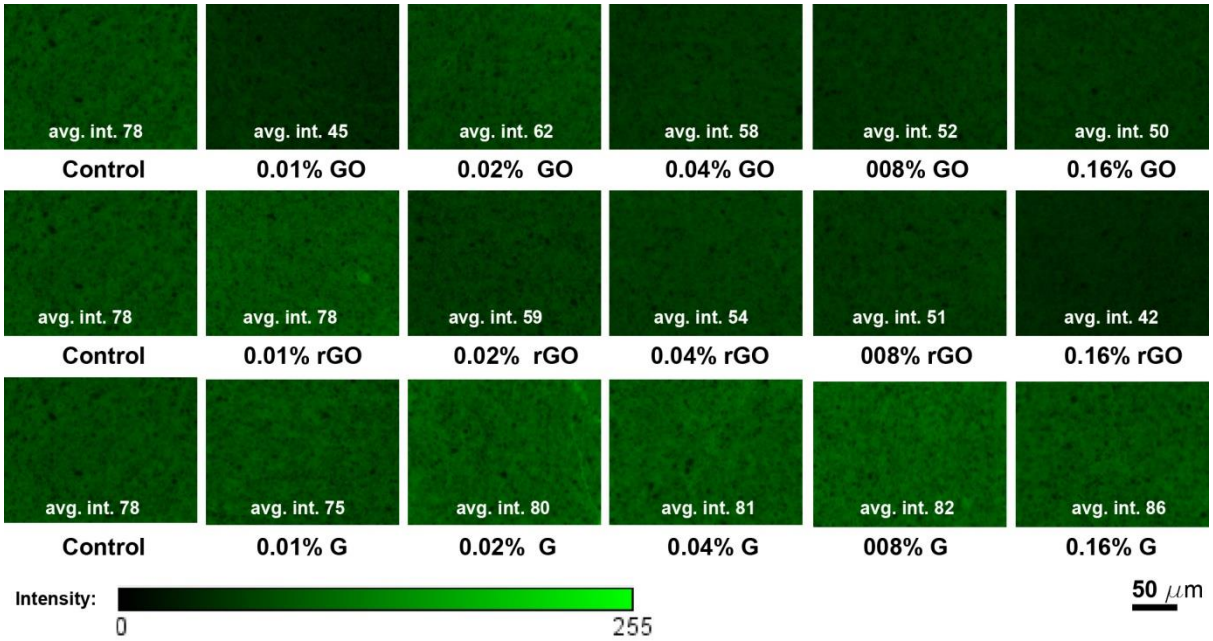

(a)

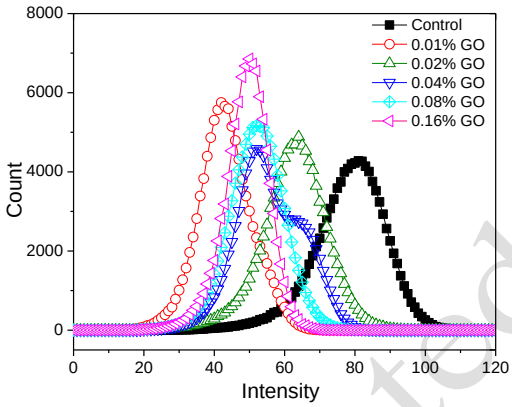

(b)

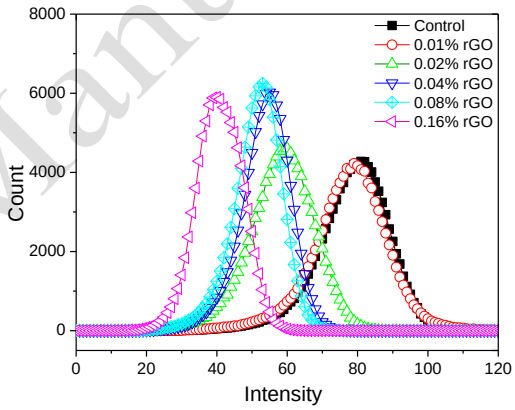

(c)

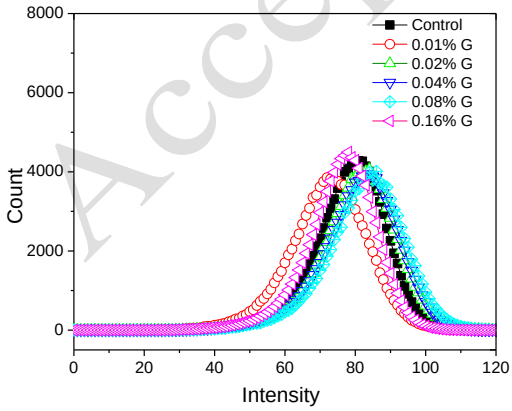

(d)

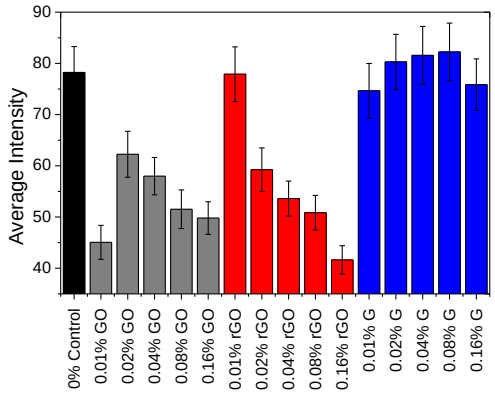

(e)

Fig. 10 Fluorescence microscopy image analysis from thin section, (a) typical images, (b) GO composites intensity distribution, (c) rGO composites intensity distribution, (d) G composites intensity distribution, and (e) average intensity.

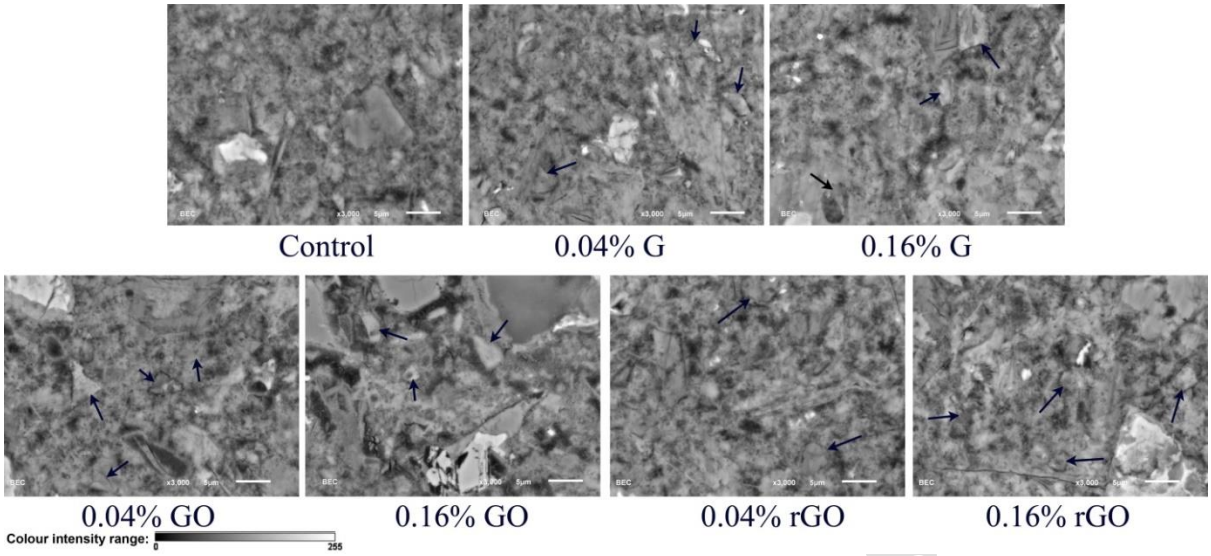

Fig. 11 SEM backscattered images of control paste and GCCs thin section after 28 days hydration.

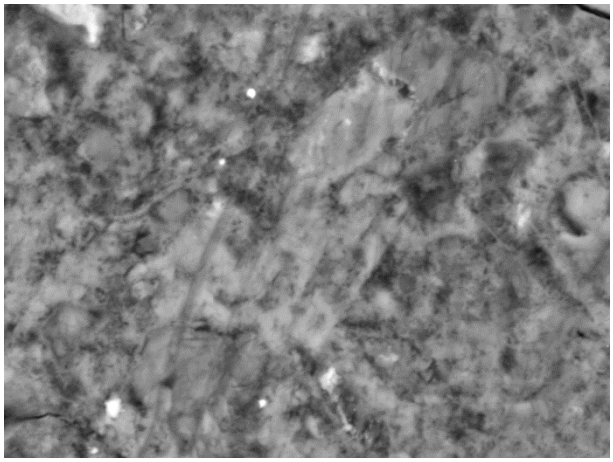

(a)

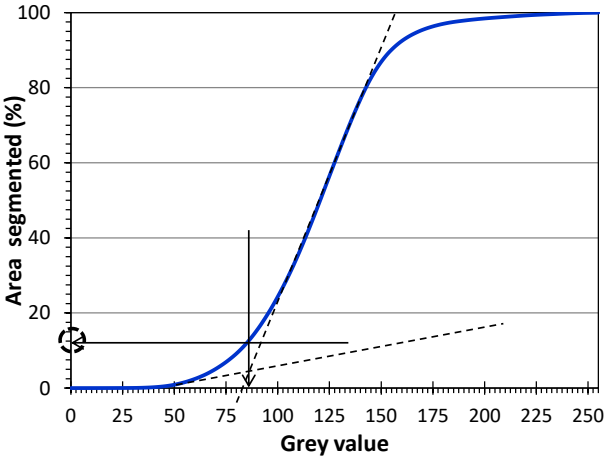

(b)

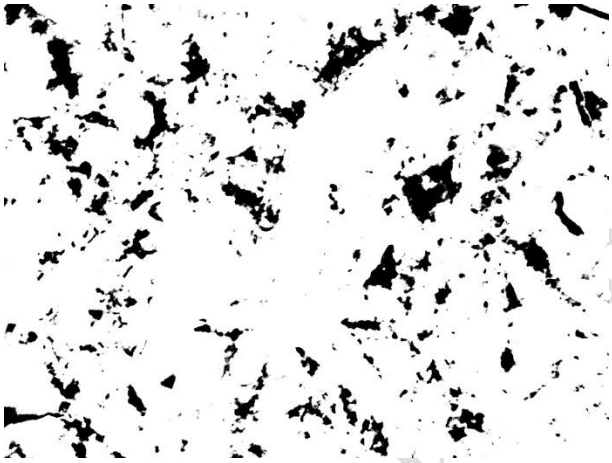

(c)

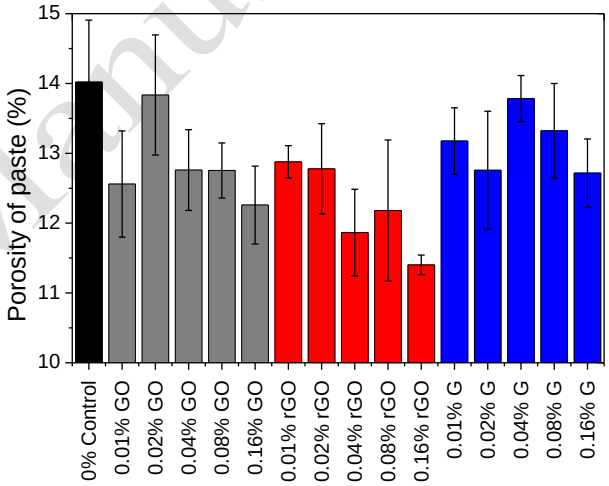

(d)

Fig. 12 Porosity of the composites from BSE images using tangent-slope thresholding method and overflow segmentation method, (a) typical BSE image of the GCCs (0.16% rGO), (b) cumulative greyscale histogram of BSE image 0.16% rGO and application of tangent-slope thresholding method, (c) pores segmented (black pixel) from 0.16% rGO at threshold level 86 indicating porosity of paste = 11.72%, and (d) average porosity of paste.

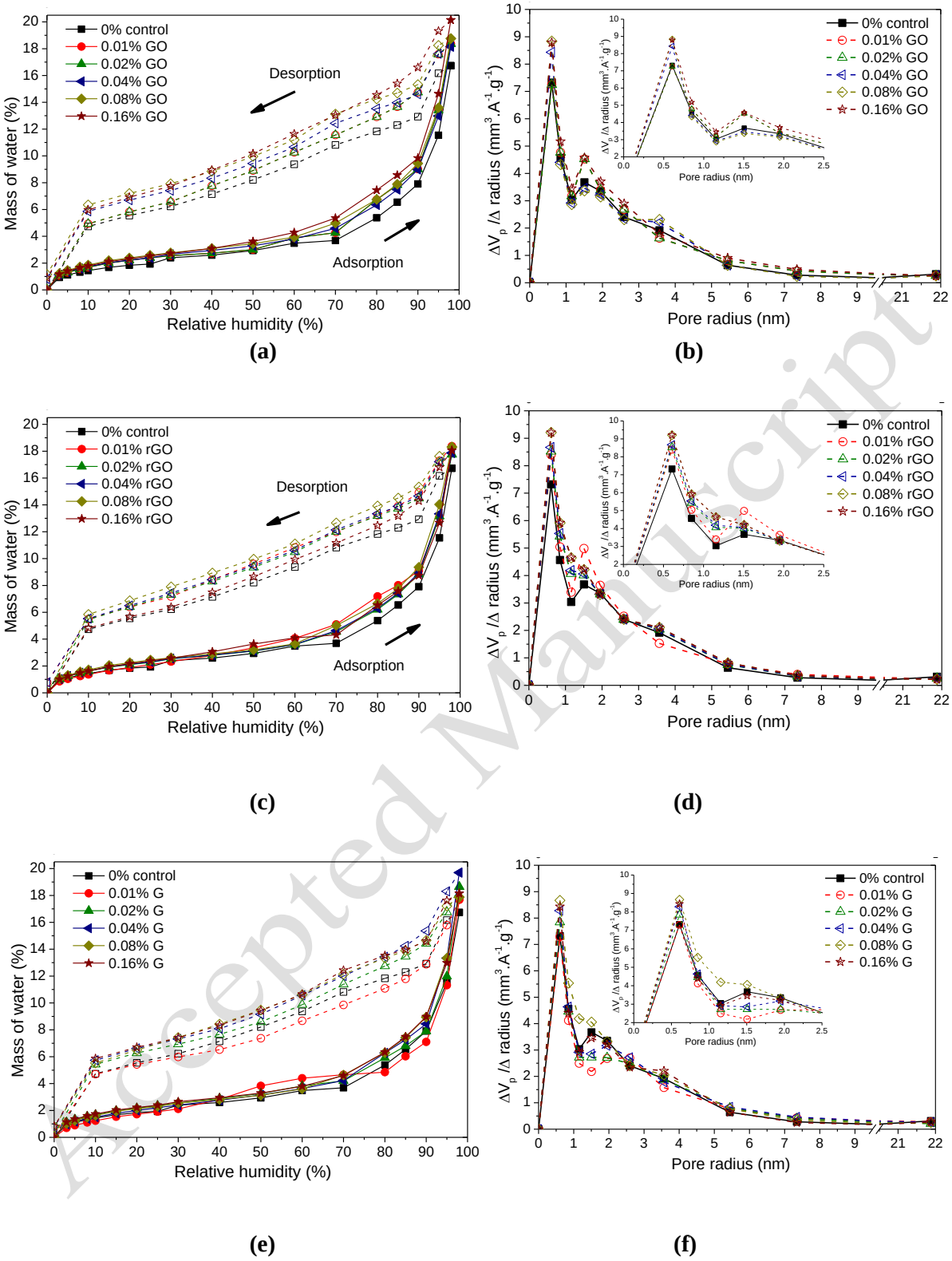

(a) **(b)**

(c) **(d)**

(e) **(f)**

Fig. 13 DVS analysis results: (a) GO composite adsorption and desorption, (b) GO composite pore volume distribution, (c) rGO composite adsorption and desorption, (d) rGO composite pore volume distribution, (e) G composite adsorption and desorption, and (f) G composite pore volume distribution.

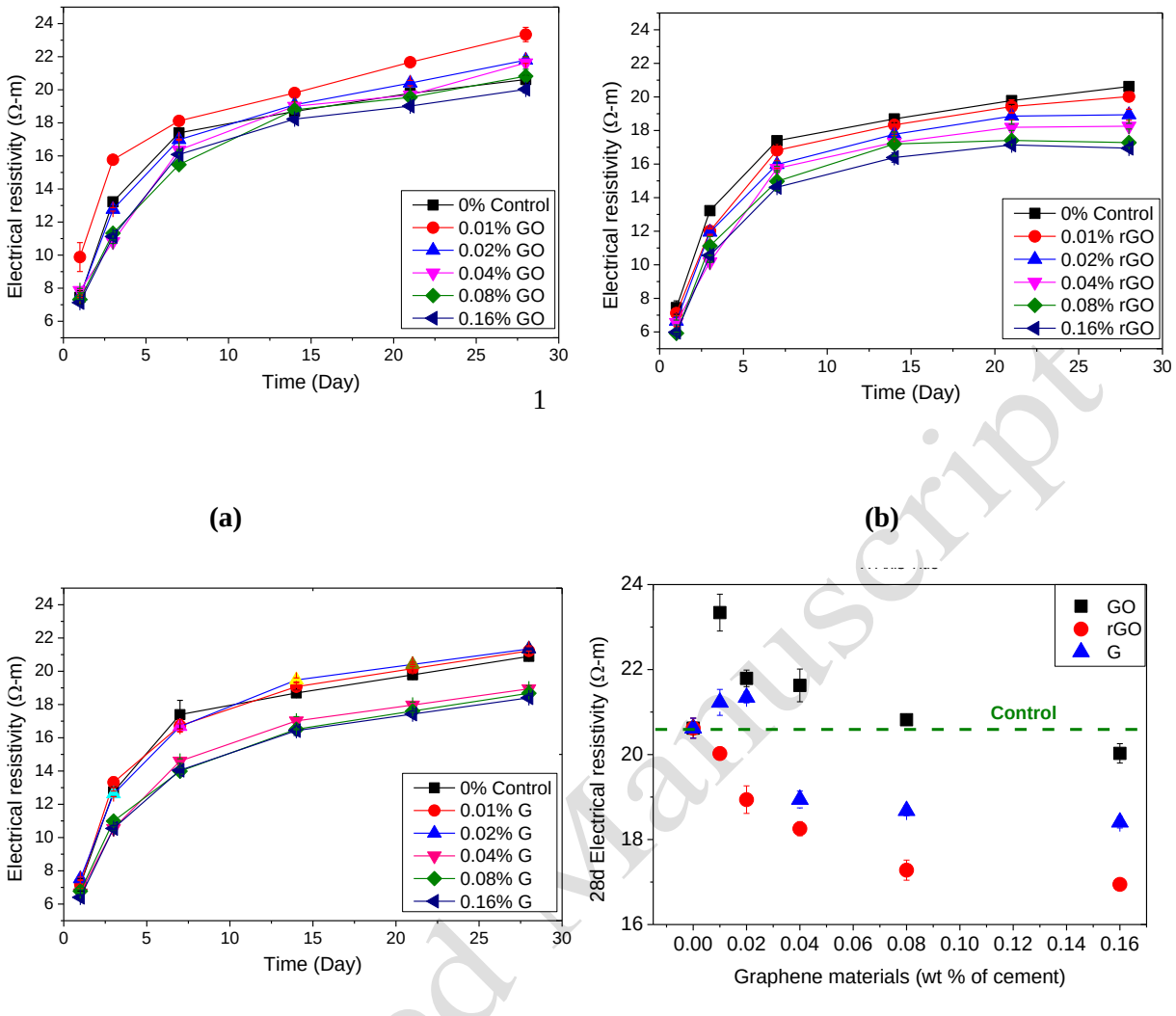

Fig. 14 Evolution of electrical resistivity, (a) GO composite, (b) rGO composite, (c) G composite, and (d) average electrical resistivity of 28-day GCCs.

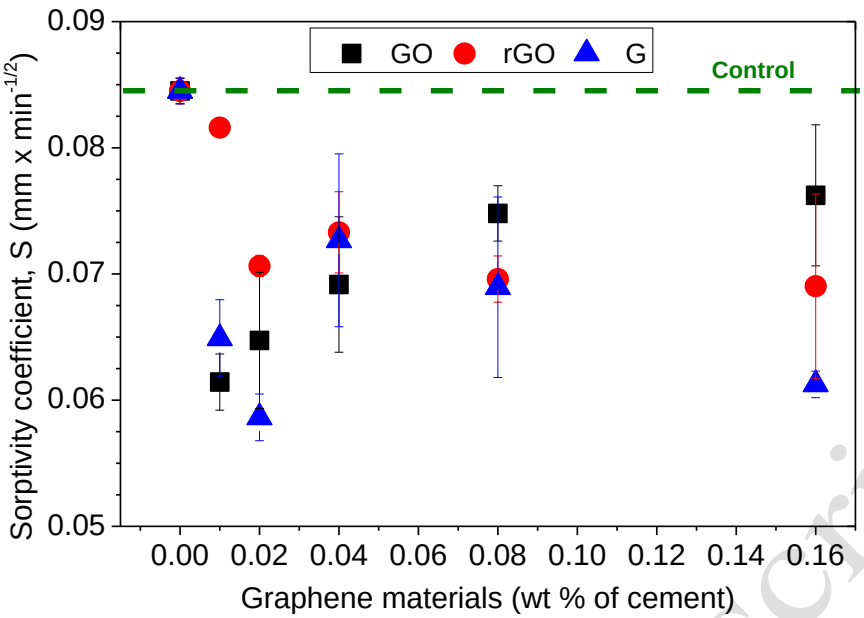

Fig. 15 Water sorptivity coefficient of 28-day GCCs.